

Electroweak phase transition in the 2HDM: Collider and gravitational wave complementarity

Dorival Gonçalves^{✉,*}, Ajay Kaladharan^{✉,†} and Yongcheng Wu^{✉,‡}

Department of Physics, Oklahoma State University, Stillwater, Oklahoma, 74078, USA

 (Received 10 February 2022; accepted 9 May 2022; published 27 May 2022)

The knowledge of the Higgs potential is crucial for understanding the origin of mass and the thermal history of our Universe. We show how collider measurements and observations of stochastic gravitational wave signals can complement each other to explore the multiform scalar potential in the two Higgs doublet model (2HDM). Accounting for theoretical and current experimental constraints, we analyze the key ingredients in the shape of the Higgs potential triggering the transmutation in phase transition, from the smooth crossover to the strong first-order phase transition ($\xi_c > 1$), focusing on the barrier formation and the upliftment of the true vacuum. In particular, we observe that the $\xi_c > 1$ regime is favored for lower scalar masses, rendering strong extra motivation for collider searches. We contrast the dominant collider signals at the HL-LHC (high-luminosity LHC) with observable gravitational wave signals at LISA. We obtain that the HL-LHC will be able to cover a vast range of the $\xi_c > 1$ parameter space, with scalar decays to heavy fermions ($H, A, H^\pm \rightarrow tt, tb$) being the most promising smoking gun signature of a strong first-order electroweak phase transition in the 2HDM.

DOI: [10.1103/PhysRevD.105.095041](https://doi.org/10.1103/PhysRevD.105.095041)

I. INTRODUCTION

The structure of the Higgs potential is deeply connected with the origin of mass and thermal history of our Universe. When the Universe was cooling down, at a temperature of order 100 GeV, it went through a transition from a symmetric phase to an electroweak (EW) broken phase, where the Higgs field(s) acquired nonvanishing vacuum expectation values. The evolution of this process strongly depends on the shape of the Higgs potential. Distinct profiles for the Higgs potential result in contrasting courses for the electroweak symmetry breaking (EWSB) in the early Universe, ranging from the smooth crossover transition in the Standard Model (SM), with the observed 125 GeV Higgs boson [1], to the strong first-order phase transition, with new physics.

The dynamics of the electroweak phase transition (EWPT) could have profound consequences for particle physics and cosmology. Most notably, it may be behind the matter and antimatter asymmetry puzzle. This asymmetry can be quantitatively featured by the baryon-to-photon ratio

measurement $n_B/n_\gamma \approx 6 \times 10^{-10}$ [2], which is several orders of magnitude larger than that expected for the symmetric scenario, indicating an asymmetry in the early Universe between baryons and antibaryons. The bulk of the antibaryons have been annihilated in the thermal history, resulting in the large present density of baryons. The ingredients required to generate the baryon asymmetry of the Universe are theoretically well understood and summarized by the three Sakharov conditions [3]. They impose that our fundamental theory displays baryon number violation C along with CP violation, and departure from thermal equilibrium. Whereas the SM satisfies baryon number and C violation, the source of CP violation from the Cabibbo-Kobayashi-Maskawa matrix is too small, and the observed Higgs mass $m_h = 125$ GeV is too high to generate the out-of-equilibrium conditions from a strong first-order phase transition [1,4]. Thus, baryogenesis requires physics beyond the SM to grant these missing ingredients. In the present work, we focus on the latter problem, generating the out-of-equilibrium conditions at the electroweak scale [5–8].

The transmutation of the EWPT pattern from the smooth crossover to the strong first-order phase transition usually requires new degrees of freedom around the EW scale, with sizable interactions with the Higgs boson [9]. Therefore, it generally accommodates beyond-the-SM scenarios with exciting phenomenological prospects, both at collider and gravitational wave (GW) experiments. At colliders, the Higgs pair production $pp \rightarrow hh$ usually plays a leading role in this discussion, as it grants a direct probe of the

*dorival@okstate.edu

†kaajay@ostatemail.okstate.edu

‡ywu@okstate.edu

Published by the American Physical Society under the terms of the Creative Commons Attribution 4.0 International license. Further distribution of this work must maintain attribution to the author(s) and the published article's title, journal citation, and DOI. Funded by SCOAP³.

Higgs potential [10–12]. It provides access to the triple Higgs coupling via nonresonant Higgs pair production, as well as to the interactions of the SM Higgs boson with new heavy scalars through resonant di-Higgs searches. The high-luminosity LHC projections indicate that the triple Higgs coupling will be bounded to $0.1 < \lambda_h^3 / \lambda_h^{\text{SM}} < 2.3$ at 95% confidence level (C.L.) [13]. Resonant searches are also a main focus, leading to significant limits [14]. Complementing the collider searches, the space-based GW experiments, such as LISA [15], will provide a new window to the Higgs potential. First-order phase transitions that emerge from a scalar field tunneling through an energy barrier in the potential generate a significant source of gravitational waves. The correspondent signal spectrum displays a characteristic peak associated with the temperature at which the phase transition occurred. For phase transitions at the EW scale, this leads to a GW spectrum around the mHz frequency, after redshifting the signal to the present time [16,17]. This prompts exciting prospects to access the nature of EWPT at LISA, as this is precisely the frequency band that this experiment is sensitive to.

In this work, we study the EWPT pattern in the two Higgs doublet model (2HDM) [18–28], where the SM is augmented by an extra doublet. Instead of focusing on benchmarks or a particular parameter space region, a general scan is performed on the theoretically and experimentally allowed parameter space. We divide our analysis into two main stages. First, we scrutinize the new physics modifications to the shape of the Higgs potential that lead to a strong first-order phase transition. We devote particular attention to the barrier formation and to the true vacuum upliftment with respect to the SM case. The obtained results work as a guide for the phenomenological studies derived in the second part of the manuscript, where we perform the respective analysis at both the HL-LHC and LISA. In this last part, besides the commonly discussed channel $A \rightarrow ZH$, other promising channels which can cover the EWPT parameter space are also investigated. These studies highlight the leading collider signatures for first-order EWPT at the LHC, as well as the complementarity of probes between collider and GW experiments.

The structure of this paper is as follows. In Sec. II, we briefly describe the 2HDM. The one-loop effective potential at finite temperature is discussed in Sec. III. It is followed by an introduction of EWPT and GW signals in Sec. IV. In Sec. V, we discuss how the shape of the potential will affect the EWPT, focusing on the barrier formation and vacuum upliftment. In Sec. VI, inspired by our shape analysis, we tailor the collider studies to the most promising channels. In addition, we derive the sensitivity to the correspondent GW signals generated in the early Universe. Finally, we summarize in Sec. VII. Some useful relations for the parameters in 2HDM are listed in the Appendix.

II. TWO HIGGS DOUBLET MODEL

The two Higgs doublet model displays one of the most minimalistic extensions of the SM that is compatible with the current experimental constraints [29]. In this work, we consider the CP -conserving 2HDM with a softly broken Z_2 symmetry.¹ The tree-level potential is given by

$$\begin{aligned} V(\Phi_1, \Phi_2) = & m_{11}^2 \Phi_1^\dagger \Phi_1 + m_{22}^2 \Phi_2^\dagger \Phi_2 - m_{12}^2 (\Phi_1^\dagger \Phi_2 + \text{H.c.}) \\ & + \frac{\lambda_1}{2} (\Phi_1^\dagger \Phi_1)^2 + \frac{\lambda_2}{2} (\Phi_2^\dagger \Phi_2)^2 + \lambda_3 (\Phi_1^\dagger \Phi_1) (\Phi_2^\dagger \Phi_2) \\ & + \lambda_4 (\Phi_1^\dagger \Phi_2) (\Phi_2^\dagger \Phi_1) + \frac{\lambda_5}{2} ((\Phi_1^\dagger \Phi_2)^2 + \text{H.c.}), \end{aligned} \quad (1)$$

where the mass terms m_{11}^2 , m_{22}^2 , and m_{12}^2 along with the couplings $\lambda_1 \dots \lambda_5$ are real parameters from Hermiticity and CP conservation. The required Z_2 symmetry, which is softly broken by m_{12}^2 , transformations $\Phi_1 \rightarrow \Phi_1$ and $\Phi_2 \rightarrow -\Phi_2$ guarantee the absence of the dangerous tree-level flavor changing neutral currents (FCNCs) [30,31]. After EWSB, the neutral components of the two $SU(2)_L$ doublets develop vacuum expectation values (VEVs). Expanding around the VEVs $\tilde{\omega}_i$, the scalar doublets Φ_i may be written as

$$\Phi_1 = \begin{pmatrix} \phi_1^+ \\ \frac{\tilde{\omega}_1 + \phi_1^0 + i\eta_1}{\sqrt{2}} \end{pmatrix} \quad \text{and} \quad \Phi_2 = \begin{pmatrix} \phi_2^+ \\ \frac{\tilde{\omega}_2 + \phi_2^0 + i\eta_2}{\sqrt{2}} \end{pmatrix}, \quad (2)$$

where the zero-temperature vacuum expectation values $v_i \equiv \tilde{\omega}_i|_{T=0}$ are connected to the SM VEV by $v_1^2 + v_2^2 = v^2 \approx (246 \text{ GeV})^2$.

The CP -conserving 2HDM leads to five physical mass eigenstates in the scalar sector: two CP -even neutral scalars h and H , a neutral CP -odd scalar A , and a charged scalar pair H^\pm . The relation between the mass and gauge eigenstates is established by the rotation angle β for the charged and CP -odd sectors, where $\tan \beta \equiv v_2/v_1$, and by the mixing angle α in the CP -even sector

$$\begin{aligned} \begin{pmatrix} G^\pm \\ H^\pm \end{pmatrix} &= \mathcal{R}(\beta) \begin{pmatrix} \phi_1^\pm \\ \phi_2^\pm \end{pmatrix}, & \begin{pmatrix} G^0 \\ A \end{pmatrix} &= \mathcal{R}(\beta) \begin{pmatrix} \eta_1 \\ \eta_2 \end{pmatrix}, \\ \begin{pmatrix} H \\ h \end{pmatrix} &= \mathcal{R}(\alpha) \begin{pmatrix} \phi_1^0 \\ \phi_2^0 \end{pmatrix}. \end{aligned} \quad (3)$$

The rotation matrix is defined as

¹Baryogenesis requires physics beyond the SM to generate new sources of CP violation and out-of-equilibrium conditions. In the present work, we focus on the latter issue.

$$\mathcal{R}(x) = \begin{pmatrix} c_x & s_x \\ -s_x & c_x \end{pmatrix}, \quad (4)$$

with $s_x \equiv \sin x$ and $c_x \equiv \cos x$. G^\pm and G^0 represent the charged and neutral massless Goldstone bosons.

Instead of the eight parameters in the Higgs potential m_{11}^2 , m_{22}^2 , m_{12}^2 , $\lambda_1 \dots \lambda_5$, a more convenient choice of parameters is

$$\tan \beta, \cos(\beta - \alpha), m_{12}^2, v, m_h, m_H, m_A, m_{H^\pm}. \quad (5)$$

The conversion between these two sets of parameters can be found in Appendix. The parameters $t_\beta \equiv \tan \beta$ and $c_{\beta-\alpha} \equiv \cos(\beta - \alpha)$ are of critical phenomenological

importance. They control the coupling strength of scalar particles to fermions and gauge bosons. Given the current experimental constraints, a particular relevant regime is the alignment limit $c_{\beta-\alpha} = 0$ [32], where the 125 GeV CP -even scalar Higgs boson couples to SM particles precisely as the SM Higgs boson.

In general, there are four types of \mathbb{Z}_2 charge assignments in the Yukawa sector that avoid FCNC at tree level. In this work, we focus on the type-I and type-II scenarios. In the first case, all fermions couple only to Φ_2 , whereas in the latter, only the up quarks couple with Φ_2 , leaving the down quarks and charged leptons to couple with Φ_1 . For both types I and II, we perform a uniform scan over the parameter space region,

$$\begin{aligned} \tan \beta &\in (0.8, 25), & m_{12}^2 &\in (10^{-3}, 10^5) \text{ GeV}^2, & m_H &\in (150, 1500) \text{ GeV}, \\ \cos(\beta - \alpha) &\in (-0.3, 0.3), & m_A &\in (150, 1500) \text{ GeV}, & m_{H^\pm} &\in (150, 1500) \text{ GeV}. \end{aligned} \quad (6)$$

The observed 125 GeV Higgs boson is identified with the h scalar. The parameter space scan is performed with SCANNERS [33,34]. Using this framework, we impose the constraints from perturbative unitarity [35–37], boundedness from below [38], vacuum stability [39,40], electroweak precision, and flavor constraints. In addition, HIGGSBOUNDS and HIGGSSIGNALS are used to incorporate the searches for additional scalars as well as the constraints from the 125 GeV Higgs boson measurements [41,42].

III. ONE-LOOP EFFECTIVE POTENTIAL AT FINITE TEMPERATURE

To study the electroweak phase transition in the early Universe, we use the loop-corrected effective potential at finite temperature. In addition to the tree-level potential V_0 from Eq. (1), the effective potential displays one-loop corrections at zero temperature from the Coleman-Weinberg potential V_{CW} and counterterms V_{CT} . Finite-temperature corrections V_T are also included. The effective potential reads

$$V_{\text{eff}} = V_0 + V_{\text{CW}} + V_{\text{CT}} + V_T. \quad (7)$$

The Coleman-Weinberg potential can be written in the Landau gauge as [43]

$$V_{\text{CW}} = \sum_i \frac{n_i}{64\pi^2} m_i^4(\Phi_1, \Phi_2) \left[\log \left(\frac{m_i^2(\Phi_1, \Phi_2)}{\mu^2} \right) - c_i \right], \quad (8)$$

where the index i sums over all particles in the thermal bath with field-dependent mass $m_i(\Phi_1, \Phi_2)$, namely, massive gauge bosons, longitudinal photon, Higgs bosons, Goldstone bosons, and fermions. n_i denotes the number

of degrees of freedom for particle i , with $n_i > 0$ for bosons and $n_i < 0$ for fermions. The various constants c_i depend on the renormalization scheme adopted. Following the $\overline{\text{MS}}$ scheme, we set c_i to 5/6 for gauge bosons and 3/2 otherwise. Finally, the renormalization scale μ is fixed at the zero-temperature VEV, $\mu = v(T=0) \approx 246 \text{ GeV}$.²

In general, the one-loop Coleman-Weinberg corrections shift the scalar masses and mixing angles with respect to the tree-level potential. To optimize our parameter scan, we adopt a renormalization prescription that enforces these parameters to match with their tree-level values [19,46]. In this setup, the counterterm part of the potential can be written as

$$\begin{aligned} V_{\text{CT}} &= \delta m_{11}^2 \Phi_1^\dagger \Phi_1 + \delta m_{22}^2 \Phi_2^\dagger \Phi_2 - \delta m_{12}^2 (\Phi_1^\dagger \Phi_2 + \text{H.c.}) \\ &+ \frac{\delta \lambda_1}{2} (\Phi_1^\dagger \Phi_1)^2 + \frac{\delta \lambda_2}{2} (\Phi_2^\dagger \Phi_2)^2 + \delta \lambda_3 (\Phi_1^\dagger \Phi_1) (\Phi_2^\dagger \Phi_2) \\ &+ \delta \lambda_4 (\Phi_1^\dagger \Phi_2) (\Phi_2^\dagger \Phi_1) + \frac{\delta \lambda_5}{2} ((\Phi_1^\dagger \Phi_2)^2 + \text{H.c.}), \end{aligned} \quad (9)$$

with the following on-shell renormalization conditions at zero temperature:

$$\partial_{\phi_i} (V_{\text{CW}} + V_{\text{CT}})|_{\omega=\omega_{\text{tree}}} = 0, \quad (10)$$

$$\partial_{\phi_i} \partial_{\phi_j} (V_{\text{CW}} + V_{\text{CT}})|_{\omega=\omega_{\text{tree}}} = 0. \quad (11)$$

The fields ϕ_i ($i = 1, \dots, 8$) denote scalar components from the Φ_1 and Φ_2 doublets, ω generically represents the ω_i

²A renormalization group improved calculation can be taken into account for a further refined estimation [44]. For the scale-dependence problem at finite temperature, we refer to Ref. [45] for a detailed discussion.

values, and ω_{tree} generically stands for the minimum of the tree-level potential for the ϕ_i fields. We followed the prescription of Ref. [46] to consistently calculate the first and second derivatives of V_{CW} . The first renormalization condition Eq. (10) imposes that the zero-temperature minimum is not shifted with respect to the tree-level value.

Similarly, the second condition Eq. (11) ensures that the zero-temperature masses and mixing angles remain the same as their tree-level assignment.

The last term in Eq. (7), the one-loop thermal corrections V_T , can be expressed as [47]

$$V_T = \frac{T^4}{2\pi^2} \left[\sum_f n_f J_+ \left(\frac{m_f^2}{T^2} \right) + \sum_{\mathcal{V}_T} n_{\mathcal{V}_T} J_- \left(\frac{m_{\mathcal{V}_T}^2}{T^2} \right) + \sum_{\mathcal{V}_L} n_{\mathcal{V}_L} J_- \left(\frac{m_{\mathcal{V}_L}^2}{T^2} \right) \right] - \frac{T^4}{2\pi^2} \sum_{\mathcal{V}_L} \frac{\pi}{6} \left(\frac{\bar{m}_{\mathcal{V}_L}^3}{T^3} - \frac{m_{\mathcal{V}_L}^3}{T^3} \right), \quad (12)$$

where the sum extends over fermions f and bosons, with the latter subdivided in transverse modes of gauge boson $\mathcal{V}_T = W_T, Z_T$ and longitudinal modes of gauge bosons and scalars $\mathcal{V}_L = W_L, Z_L, \gamma_L, \Phi^0, \Phi^\pm$. The resummation of the $n = 0$ Matsubara modes of \mathcal{V}_L result in thermal corrections to their masses [48,49]. The second line in Eq. (12) indicates the Daisy contributions, where $\bar{m}_{\mathcal{V}_L}$ is the thermal Debye mass following the Arnold-Espinosa scheme [19,47]. Lastly, the thermal functions for fermions (J_+) and for bosons (J_-) read

$$J_\pm(x) = \mp \int_0^\infty dy y^2 \log(1 \pm e^{-\sqrt{y^2+x^2}}). \quad (13)$$

While the effective potential displays theoretical uncertainties arising from the choice of gauge parameter [44,50–54], gauge-independent probes can be constructed exploiting the Nielsen identities [55]. These identities state that the gauge dependence vanishes at the extrema of the potential

$$\frac{\partial V_{\text{eff}}(\Phi_1, \Phi_2, \xi)}{\partial \xi} = -C_i(\Phi_1, \Phi_2, \xi) \frac{\partial V_{\text{eff}}(\Phi_1, \Phi_2, \xi)}{\partial \phi_i}, \quad (14)$$

where ξ is the gauge fixing parameter. This motivates us to adopt two distinct methods in our manuscript for the phenomenological analyses. The first approach encompasses the calculation of the finite-temperature effective potential and the subsequent numerical scan. The second one focuses on the calculation of the vacuum upliftment at $T = 0$. As we will highlight in Sec. VB, the upliftment of the true vacuum with respect to the symmetric one at zero temperature works as an effective probe to the strength of phase transition. Whereas the first method displays uncertainties rooted in the choice of gauge parameter, the latter approach is gauge invariant, as guaranteed by the Nielsen identities [22,50]. Notice that we introduce extra counterterms to preserve the position of the EW vacuum, as well as the masses, at one-loop order. The phenomenological agreement between our numerical scan with the profile derived from the vacuum upliftment will, in particular,

evidence that the numerical scan is well grounded, despite its uncertainties.³

IV. ELECTROWEAK PHASE TRANSITION AND GRAVITATIONAL WAVES

The effective potential at finite temperature determines the dynamics of the phase transition. The two Higgs doublet model exhibits multiple phase transition processes. For successful baryogenesis, the sphaleron process inside the bubble should be heavily suppressed to prevent the net baryon number generated around the bubble wall from significant washout. This condition requires that the EWPT be of strong first order [49]

$$\xi_c \equiv \frac{v_c}{T_c} \gtrsim 1, \quad (15)$$

where $v_c \equiv \sqrt{\omega_1^2 + \omega_2^2}|_{T_c}$ is the Higgs VEV at the critical temperature T_c , which is defined when the would-be true vacuum and false vacuum are degenerate. The approximate inequality denotes the theoretical uncertainty in this condition [50].

The transition from false to true vacuum takes place via thermal tunneling. It results in the formation of bubbles of the broken phase that expand in the surrounding region of symmetric phase, converting the false vacuum into true vacuum. The tunneling probability can be written as [56,57]

$$\Gamma(T) \approx T^4 \left(\frac{S_3}{2\pi T} \right)^{3/2} e^{-\frac{S_3}{T}}, \quad (16)$$

where S_3 is the three-dimensional Euclidean action corresponding to the critical bubble

³Note that when the coupling in the scalar potential is large, as usually required by a strong first-order phase transition, one should check the reliability of the perturbative calculations. Lattice simulations for 2HDM are performed for two particular benchmark points in Ref. [24], where the authors made comparisons among different methods. It is shown that the perturbative estimation of the strength of the phase transition $\xi_c \equiv v_c/T_c$ is close to the lattice results.

$$S_3 = 4\pi \int_0^\infty dr r^2 \left[\frac{1}{2} \left(\frac{d\phi(r)}{dr} \right)^2 + V(\phi, T) \right]. \quad (17)$$

Here, the scalar field ϕ is the bubble profile of the critical bubble. It is obtained as a solution to the following differential equation:

$$\frac{d^2\phi}{dr^2} + \frac{2}{r} \frac{d\phi}{dr} = \frac{dV(\phi, T)}{d\phi}, \quad \text{with} \quad \lim_{r \rightarrow \infty} \phi(r) = 0 \quad \text{and} \\ \lim_{r \rightarrow 0} \frac{d\phi(r)}{dr} = 0. \quad (18)$$

We use the publicly available code COSMOTRANSITIONS to solve the differential equation and compute the Euclidean action S_3 [58].

The first-order phase transition completes around nucleation temperature T_n , where one bubble nucleates per unit volume [59]

$$\int_{T_n}^\infty \frac{dT}{T} \frac{\Gamma(T)}{H(T)^4} = 1. \quad (19)$$

This ensures that the bubbles percolate even in the inflating universe. For the electroweak phase transition, the above condition can be roughly approximated as [49]

$$\frac{S_3(T)}{T} \approx 140. \quad (20)$$

One of the important consequences of the strong first-order EWPT is the production of stochastic gravitational waves. The GW signals from phase transition have three main sources: collision of the vacuum bubbles, sound waves, and turbulence in the plasma. For each source, the GW spectrum can be expressed as numerical functions in terms of two important parameters determined from the phase transition dynamics [16,60]. The first parameter is $\alpha \equiv \epsilon/\rho_{\text{rad}}$, the latent heat released in the phase transition (ϵ) to the radiation energy density (ρ_{rad}). The latent heat ϵ and ρ_{rad} are obtained from

$$\epsilon = \Delta \left(-V_{\text{eff}} + T \frac{\partial V_{\text{eff}}}{\partial T} \right)_{T=T_n} \quad \text{and} \quad \rho_{\text{rad}} = \frac{\pi^2}{30} g_* T_n^4, \quad (21)$$

where Δ means the difference between the stable and metastable minima, and g_* is the number of relativistic degrees of freedom in the plasma. The second key parameter characterizing the spectrum of gravitational waves is the inverse time duration of the phase transition β/H_n . This quantity is defined as

$$\frac{\beta}{H_n} \equiv T_n \frac{d}{dT} \left(\frac{S_3}{T} \right) \Big|_{T=T_n}, \quad (22)$$

where H_n denotes the Hubble constant at the nucleation temperature T_n . Strong GW signals are typically associated

with large latent heat release (large α) and slow phase transition (small β/H_n).

Finally, to estimate the sensitivity of GW experiments, we adopt the signal-to-noise ratio (SNR) measure [60]

$$\text{SNR} = \sqrt{\mathcal{T} \int_{f_{\text{min}}}^{f_{\text{max}}} df \left[\frac{h^2 \Omega_{\text{GW}}(f)}{h^2 \Omega_{\text{Sens}}(f)} \right]^2}, \quad (23)$$

where Ω_{Sens} is the sensitive curve of the considered GW experiment [15], and \mathcal{T} is associated with the duration of the mission. In the present study, we focus on the LISA experiment as a benchmark, assuming $\mathcal{T} = 5$ years and the threshold of detection as $\text{SNR} = 10$ [60].

V. THE SHAPE OF THE HIGGS POTENTIAL

The extension of the SM Higgs sector with another Higgs doublet in the 2HDM can promote the phase transition pattern from a smooth crossover to a strong first-order phase transition.⁴ To study the key ingredients triggering this transmutation in the EWPT, we need to probe the shape and thermal evolution of the effective potential. In this section, we focus on the barrier formation and the upliftment of the true vacuum [22,61,62]. The parameter space analysis is organized based on the most relevant components of the effective potential generating these changes in the profile of the Higgs potential [63]. This characterization is used as a key ingredient to pin down the leading phenomenological parameters for strong first-order phase transition.

In our studies, we focus on the type-I and -II scenarios for the Yukawa couplings. The main difference between these two cases in the effective potential comes from the bottom Yukawa coupling in the Daisy terms. In terms of phase transition, these two scenarios result in negligible differences. In Fig. 1, we show the ratio of ξ_c between type I and II as a function of t_β using the same input parameters. We focus on the points that satisfy all the current constraints for both scenarios. We observe depleted differences between ξ_c^I and ξ_c^{II} with most points differing only in the subpercent level. While there is a small enhancement for the ratio ξ_c^I/ξ_c^{II} toward larger t_β (as in type II, the Daisy contributions result in a slightly deeper potential at the true vacuum), the difference is phenomenologically insignificant. Since the considered scenarios display a similar phase transition profile, with only subleading differences, we will mostly focus on the type-I case in the present section. Nevertheless, when we discuss the experimental sensitivities, we will show the results for both scenarios as they can present distinct collider phenomenology due to their different fermionic couplings.

⁴In our study, we focus on one-step electroweak symmetry breaking, refraining to address the multistep phase transition, which turns out to be far more rare in the 2HDM.

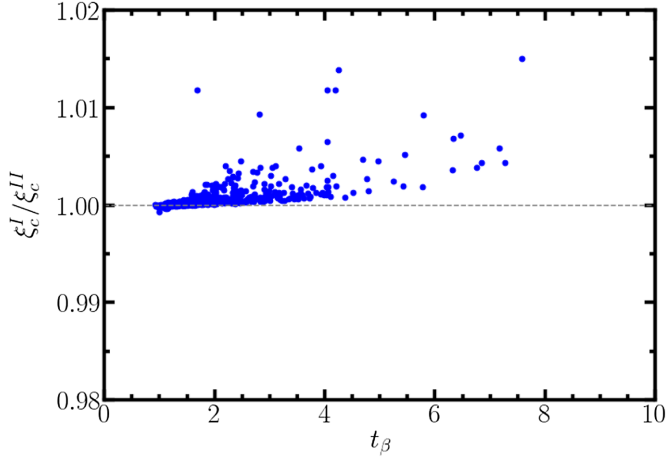


FIG. 1. The ratio of order parameter ξ_c between the type-I and II 2HDM as a function of t_β . The considered points display strong first-order phase transition $\xi_c > 1$. We focus on the points that satisfy all the current constraints for both scenarios. See Sec. II for more details on the parameter space scan.

A. Barrier formation

Moving forward, we scrutinize the 2HDM phase transition pattern, analyzing three classes of contributions to the potential barrier: tree-level (V_0), one-loop ($V_1 \equiv V_{\text{CW}} + V_{\text{CT}}$), and thermal effects (V_T). Our main target is to identify which of these terms plays a crucial role in introducing the barrier between the broken and unbroken vacua, granting the possibility of strong first-order electro-weak phase transition (SFOEWPT) in the 2HDM [63]. The correlations among these contributions to the potential barrier are presented in Fig. 2. For illustration, we focus on the type-I 2HDM with $\xi_c > 1$. The barrier of the potential is the position where the effective potential

obtains the maximum value in the tunneling path obtained by solving Eq. (18). We defined the height of the barrier as the difference between the effective potential at the barrier and false vacuum. The position of the barrier at T_c is approximated by the point where the potential attains maximum value in the line connecting the true and false vacua. We observe that the potential barrier in the 2HDM is dominantly generated by a coalition between the one-loop and thermal components. These terms display positive contributions to the potential barrier δV_1^b , $\delta V_T^b > 0$ for 99% of the parameter space points. In contrast, the tree-level term V_0 typically works against the barrier formation.

In Fig. 3 (left panel), we present the fraction between the two leading terms to the potential barrier as a function of the order parameter ξ_c . We focus on the region with positive contributions δV_1^b , $\delta V_T^b > 0$ enclosing the bulk of the parameter space points. Two comments are in order. First, in the strong first-order phase transition regime $\xi_c > 1$, the phase transition is mostly one-loop driven; i.e., the effective potential barrier is dominantly generated by the one-loop term. In this case, the \hbar loop corrections can generate relevant nonpolynomial field dependences, such as $h^4 \ln h^2$, that contribute to the barrier formation [63,64]. Second, if the fraction of the barrier height provided by the one-loop contribution is close to 100%, the tunneling from the false vacuum (metastable vacuum) to the true vacuum is more challenging. For this reason, the universe with $\xi_c \gtrsim 2.5$ is trapped in the false vacuum and electroweak symmetry breaking does not occur. We should notice that this feature is associated with the dominant phase space regime δV_1^b , $\delta V_T^b > 0$. Conversely, the rarer tree-level or thermally driven setup can still generate stronger phase transition $\xi_c \gtrsim 2.5$.

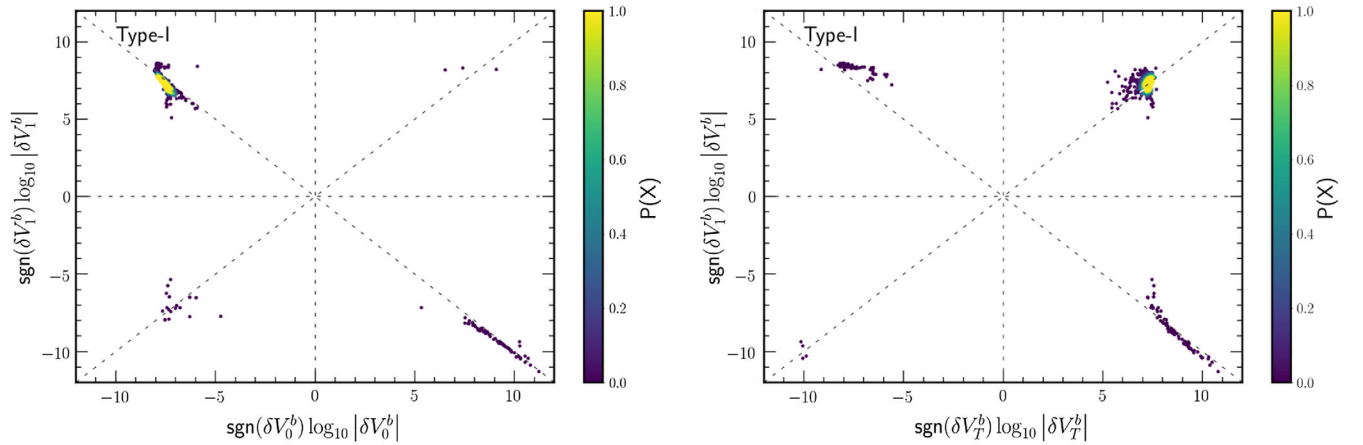


FIG. 2. Left panel: contribution of the tree-level potential to the barrier (V_0^b) against the one-loop corrections (V_1^b). Right panel: thermal contributions to the barrier (V_T^b) against the one-loop corrections (V_1^b). The regions are color coded with the probability density of points. We consider the type-I 2HDM requiring $\xi_c > 1$.

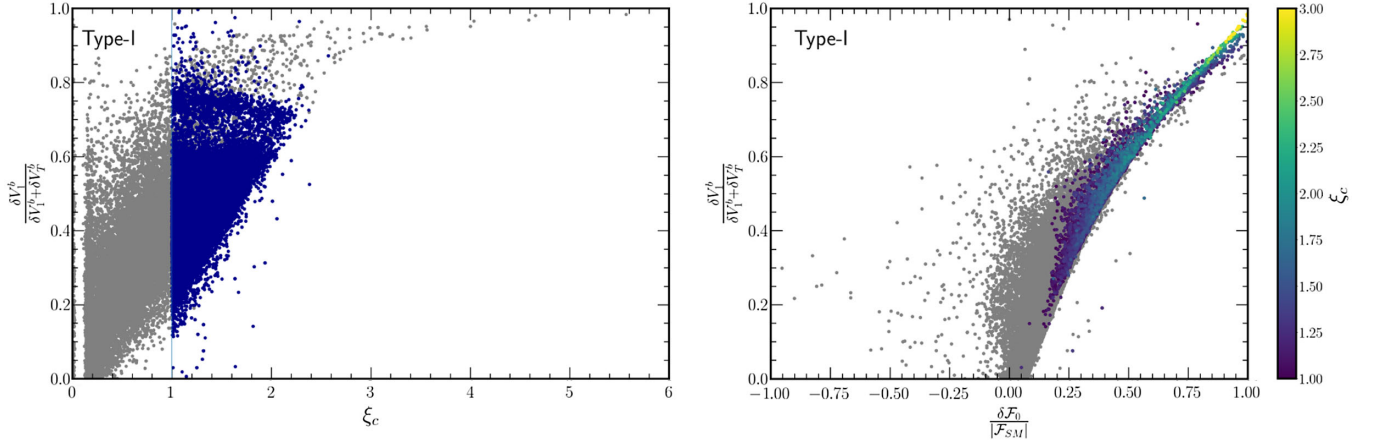


FIG. 3. Left panel: the ratio $\frac{\delta V_1^b}{\delta V_1^b + \delta V_T^b}$ for the barrier at T_c versus ξ_c . Blue denotes the points with $\xi_c > 1$ and have nucleation temperature, while gray represents points with first-order phase transition. Right panel: the ratio $\frac{\delta V_1^b}{\delta V_1^b + \delta V_T^b}$ for the barrier at T_c versus $\delta \mathcal{F}_0 / \mathcal{F}_0^{\text{SM}}$ color coded with ξ_c . Gray denotes all first-order phase transition points. We assume the type-I 2HDM, focusing on the most probable region in Fig. 2, where the barrier is generated by the one-loop and thermal corrections $\delta V_1^b, \delta V_T^b > 0$.

B. Vacuum upliftment

After looking at the general new physics contributions producing the barrier, we now focus on the effects on the potential at the vacua. It has been shown that the strength of the phase transition is correlated with the upliftment of the true vacuum compared to the symmetric one at zero temperature [22,61,62]. If the Higgs potential is shallow at $T = 0$, the required thermal upliftment for SFOEWPT, making the true vacuum degenerate with the false one, is reduced. Following a similar notation to Ref. [22], we define a dimensionless parameter to measure the true vacuum upliftment

$$\frac{\Delta \mathcal{F}_0}{|\mathcal{F}_0^{\text{SM}}|} \equiv \frac{\mathcal{F}_0 - \mathcal{F}_0^{\text{SM}}}{|\mathcal{F}_0^{\text{SM}}|}, \quad (24)$$

where \mathcal{F}_0 is the vacuum energy density of the 2HDM at $T = 0$ defined as

$$\mathcal{F}_0 \equiv V_{\text{eff}}(v_1, v_2, T = 0) - V_{\text{eff}}(0, 0, T = 0), \quad (25)$$

and $\mathcal{F}_0^{\text{SM}} = -1.25 \times 10^8 \text{ GeV}^4$. In Fig. 3 (right panel), we note that the barrier height provided by the one-loop contribution is correlated with $\Delta \mathcal{F}_0 / |\mathcal{F}_0^{\text{SM}}|$, which measures the vacuum upliftment at zero temperature. The larger the one-loop contribution, the higher the vacuum upliftment. This correlation is especially prominent for $\xi_c > 1$. Since the one-loop effects are dominant with respect to thermal corrections for $\xi_c > 1$, $\Delta \mathcal{F}_0 / |\mathcal{F}_0^{\text{SM}}|$ works as a good first approximation to study some general properties of the EWPT, even though it is a zero-temperature quantity. In particular, it is possible to define a typically necessary condition for a first-order phase transition with the minimum threshold $\Delta \mathcal{F}_0 / |\mathcal{F}_0^{\text{SM}}| > 0.34$ [22]. Although this condition encapsulates most of the $\xi_c > 1$ points, we should note from Fig. 3 that it does not work as a sufficient requirement for SFOEWPT.

While $\Delta \mathcal{F}_0 / |\mathcal{F}_0^{\text{SM}}|$ does not provide a one-to-one correlation with the strength of EWPT, it is helpful to explain critical features of the 2HDM parameter space. In the alignment limit, the important contributions to \mathcal{F}_0 come from H , A , and H^\pm , which can be written as

$$\begin{aligned} \mathcal{F}_0^{1,H}(c_{\beta-\alpha}=0) &= \frac{1}{512\pi^2} \left[\left(3m_h^2 + 2m_H^2 - 6\frac{m_{12}^2}{s_\beta c_\beta} \right) \left(m_h^2 + 2m_H^2 - 2\frac{m_{12}^2}{s_\beta c_\beta} \right) + \left(m_h^2 - 2\frac{m_{12}^2}{s_\beta c_\beta} \right)^2 \log \left(\frac{4m_H^4}{(m_h^2 - 2m_{12}^2/(s_\beta c_\beta))^2} \right) \right], \\ \mathcal{F}_0^{1,A}(c_{\beta-\alpha}=0) &= \frac{1}{512\pi^2} \left[\left(3m_h^2 + 2m_A^2 - 6\frac{m_{12}^2}{s_\beta c_\beta} \right) \left(m_h^2 + 2m_A^2 - 2\frac{m_{12}^2}{s_\beta c_\beta} \right) + \left(m_h^2 - 2\frac{m_{12}^2}{s_\beta c_\beta} \right)^2 \log \left(\frac{4m_A^4}{(m_h^2 - 2m_{12}^2/(s_\beta c_\beta))^2} \right) \right], \\ \mathcal{F}_0^{1,H^\pm}(c_{\beta-\alpha}=0) &= \frac{1}{256\pi^2} \left[\left(3m_h^2 + 2m_{H^\pm}^2 - 6\frac{m_{12}^2}{s_\beta c_\beta} \right) \left(m_h^2 + 2m_{H^\pm}^2 - 2\frac{m_{12}^2}{s_\beta c_\beta} \right) + \left(m_h^2 - 2\frac{m_{12}^2}{s_\beta c_\beta} \right)^2 \log \left(\frac{4m_{H^\pm}^4}{(m_h^2 - 2m_{12}^2/(s_\beta c_\beta))^2} \right) \right]. \end{aligned} \quad (26)$$

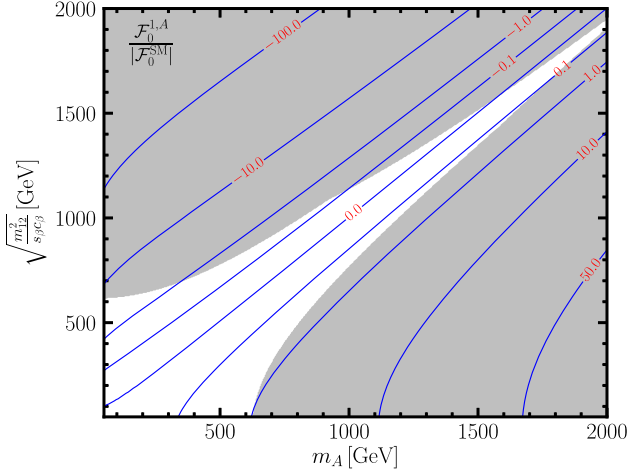


FIG. 4. The individual contribution $\mathcal{F}_0^{1,A}/|\mathcal{F}_0^{\text{SM}}|$ from A (blue solid line) in the $m_A - \sqrt{\frac{m_{12}^2}{s_\beta c_\beta}}$ plane. The contributions from H and H^\pm have the same form. The number in red inside each line indicates the value for $\mathcal{F}_0^{1,A}/|\mathcal{F}_0^{\text{SM}}|$. We assume the alignment limit. The gray shaded region is excluded by unitarity and perturbativity constraints assuming $t_\beta = 1$, $c_{\beta-\alpha} = 0$, and $m_A = m_{H^\pm} = m_H + 100$ GeV.

Using these expressions, we can write the shift in vacuum energy density with respect to the SM value with

$$\Delta\mathcal{F}_0 = \mathcal{F}_0 - \mathcal{F}_0^{\text{SM}} = \mathcal{F}_0^{1,H} + \mathcal{F}_0^{1,A} + \mathcal{F}_0^{1,H^\pm}. \quad (27)$$

Remarkably, the individual contributions from H , A , and H^\pm to \mathcal{F}_0 are of the same form. Thus, in this sense, there should be no difference in the preferred region in terms of m_H , m_A , and m_{H^\pm} . On the other hand, $m_{12}^2/(s_\beta c_\beta)$ also plays an important role. In Fig. 4, the individual contributions from A to \mathcal{F}_0 are shown (H and H^\pm have the same form), from which it is easy to find that $\mathcal{F}_0^{1,\Phi}$ will be negative when $m_{12}/\sqrt{s_\beta c_\beta}$ is larger than the scalar mass m_Φ , where $\Phi = H, A$, or H^\pm . The larger the difference is, the more negative it will be. Contrarily, when the scalar mass is larger than $m_{12}/\sqrt{s_\beta c_\beta}$, \mathcal{F}_0 will tend to be positive, uplifting the true vacuum, and favoring the strong first-order phase transition. However, the vacuum upliftment $\Delta\mathcal{F}_0$ is limited from above and below by perturbative unitarity constraints [37]. For illustration, as a benchmark, we denote the perturbative unitarity constraints as the gray shaded region in Fig. 4 for $t_\beta = 1$, $c_{\beta-\alpha} = 0$, and $m_A = m_{H^\pm} = m_H + 100$ GeV. As the allowed region (unshaded area) becomes narrower toward larger scalar masses and $m_{12}/\sqrt{s_\beta c_\beta}$, sizable scalar masses admit only a small vacuum upliftment $\Delta\mathcal{F}_0$. Therefore, SFOEWPT generally favors low scalar masses, granting a larger (and positive) $\Delta\mathcal{F}_0$. These analytical results are in accordance with the

rather general arguments from Ref. [9], in which the author also argued that light scalars are favored.

It is possible to shed more light on the general profile of EWPT in the 2HDM, combining the \mathcal{F}_0 dependence on the new scalar masses with the constraints from electroweak precision measurements, which require either m_H or m_A to be close to m_{H^\pm} . In Fig. 5, we show the scanned points in the $(\Delta m_H, \Delta m_A)$ plane, where $\Delta m_H \equiv m_H - m_{H^\pm}$ and $\Delta m_A \equiv m_A - m_{H^\pm}$. The heat map tracks ξ_c (left two panels) and the SNR (right two panels). For the study in terms of the order parameter ξ_c (left panels), the black points represent the parameter space regime with first-order phase transition with $\xi_c > 0$. In contrast, for the SNR analysis (right panels), the black points characterize the regime with $\xi_c > 1$. The gray points in the background pass all the theoretical and current experimental constraints. The results display a general cross pattern in the $(\Delta m_H, \Delta m_A)$ plane dominantly induced by the electroweak precision measurements [65,66]. There are significant differences between the type-I and -II scenarios, prompted by the flavor physics constraints. More concretely, bounds from B-meson decays require $m_{H^\pm} \gtrsim 580$ GeV in type-II 2HDM. In particular, this lower bound on the charged scalar mass cuts off part of the top and right $(\Delta m_H, \Delta m_A)$ branches compared with the type-I scenario. The type-I and -II 2HDMs present a similar phase transition profile for the remaining parameter space points, as shown in Fig. 1.

Before discussing the phase transition pattern presented in Fig. 5, we would like to point out several theoretical constraints that will be important for our analysis. Especially, we want to highlight that $m_{12}/\sqrt{s_\beta c_\beta}$ cannot be too different from the scalar masses. First, we consider the perturbative constraints. We start by writing the λ_1 and λ_2 couplings in the alignment limit

$$\begin{aligned} \lambda_1 v^2 &\approx m_h^2 + t_\beta^2 \left(m_H^2 - \frac{m_{12}^2}{s_\beta c_\beta} \right), \\ \lambda_2 v^2 &\approx m_h^2 + \frac{1}{t_\beta} \left(m_H^2 - \frac{m_{12}^2}{s_\beta c_\beta} \right). \end{aligned} \quad (28)$$

Because of their strong t_β dependence, perturbativity limits for λ_1 and λ_2 demand $m_H^2 \approx m_{12}^2/(s_\beta c_\beta)$ for t_β significantly different from 1. Second, the boundedness from below limits [38] $\lambda_{1,2} > 0$ requires that $m_{12}^2/(s_\beta c_\beta)$ cannot be much larger than m_H^2 .

Exploring the aforementioned theoretical constraints and the scalar contributions to \mathcal{F}_0 , we scrutinize the general phase transition profile shown Fig. 5 by looking at each of the $(\Delta m_H, \Delta m_A)$ branches.

- (i) $m_H < m_{H^\pm} \approx m_A$ (left branch): This mass configuration displays numerous first-order phase transition points. Since $m_{12}^2/(s_\beta c_\beta)$ cannot be significantly larger than m_H^2 , this leads to large and positive contributions from A and H^\pm to \mathcal{F}_0 associated with

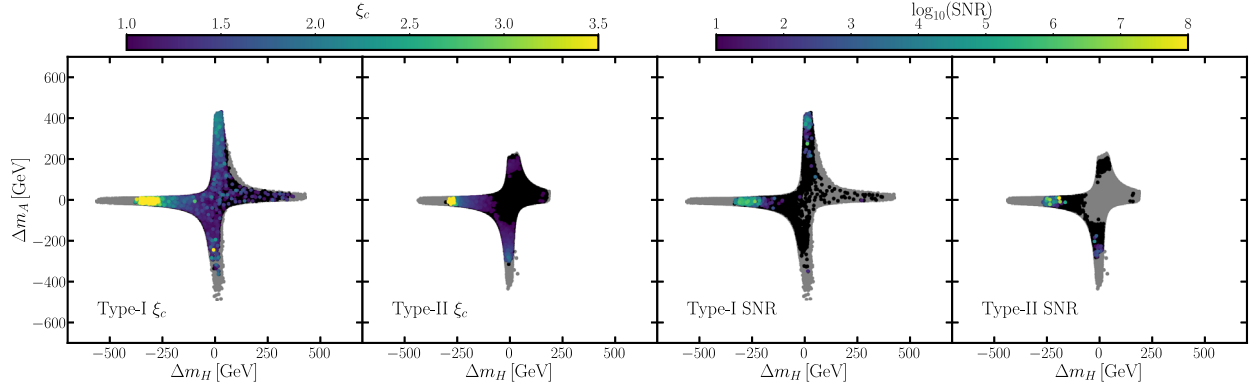


FIG. 5. Parameter space scan in terms of $(\Delta m_H, \Delta m_A)$. The heat map tracks ξ_c (left two panels) and the SNR (right two panels). For the study in terms of the order parameter ξ_c (left two panels), the black points represent the parameter space regime with first-order phase transition with $\xi_c > 0$. In contrast, for the SNR analysis (right two panels), the black points characterize the regime with $\xi_c > 1$. The parameter space scan is performed with SCANNERS [34], where we impose the constraints from perturbative unitarity, boundedness from below, vacuum stability, electroweak precision, and flavor constraints. HIGGSBOUNDS and HIGGSIGNALS are used to incorporate the searches for additional scalars as well as the 125 GeV Higgs boson measurements [41,42]. For more details on the parameter space scan, see Sec. II.

typically small effects from H . These properties promote the $m_H < m_{H^\pm} \approx m_A$ regime as one of the most likely configurations to achieve SFOEWPT in the 2HDM. Further, when the mass difference $|\Delta m_H|$ is large, the contributions to \mathcal{F}_0 from H^\pm and A are also sizable. Hence, large $|\Delta m_H|$ is more likely to grant SFOEWPT.⁵ Remarkably, this results in important phenomenological consequences for LHC searches. In particular, it favors new physics searches via the $A \rightarrow ZH$ channel that will be discussed in Sec. VI B.

- (ii) $m_H \approx m_{H^\pm} < m_A$ (top branch): This regime also presents a sizable number of $\xi_c > 1$ points. As $m_{12}^2/(s_\beta c_\beta)$ cannot be much larger than m_H^2 , the leading positive contribution to \mathcal{F}_0 arises from the pseudoscalar A . In addition, when $m_{12}^2/(s_\beta c_\beta)$ is smaller than $m_{H(H^\pm)}^2$, H (H^\pm) can also contribute positively, while at a subleading level when compared to A . Hence, the order parameter ξ_c tends to be slightly suppressed in comparison to the left branch. Finally, due to similar arguments as for the left branch, sizable $|\Delta m_A|$ is more likely to yield SFOEWPT.
- (iii) $m_H \approx m_{H^\pm} > m_A$ (bottom branch): This region can provide SFOEWPT, as long as $m_{12}^2/(s_\beta c_\beta)$ is much lower than $m_H^2 \approx m_{H^\pm}^2$. In this regime, the constraints from $\lambda_{1,2}$ imply $t_\beta \rightarrow 1$ to generate a large-order parameter $\xi_c > 1$.

- (iv) $m_H > m_{H^\pm} \approx m_A$ (right branch): This mass configuration renders a suppressed number of first-order phase transition points. Similar to the bottom branch, $m_{12}^2/s_\beta c_\beta$ has to be much lower than m_H^2 to achieve the $\xi_c > 1$ regime. However, in this parameter space, only H can contribute significantly to \mathcal{F}_0 , which leads to a lower chance to achieve SFOEWPT.
- (v) $m_H \approx m_{H^\pm} \approx m_A$ (central region): This region has a depleted number of SFOEWPT points. All the considered masses are close to each other, as well as $m_{12}/\sqrt{s_\beta c_\beta}$. Thus, all their contributions to \mathcal{F}_0 will be suppressed. Notably, due to the charged Higgs mass constraint $m_{H^\pm} > 580$ GeV, the type-II 2HDM displays further suppression on the number of $\xi_c > 1$ points for this region in comparison to the type I.

Combining all these arguments, we find that (i) $m_H < m_{H^\pm} \approx m_A$ provides the most likely regime to accommodate first-order EWPT, (ii) $m_H \approx m_{H^\pm} < m_A$, followed by $m_H \approx m_{H^\pm} > m_A$, also have a large chance to provide $\xi_c > 1$, and (iii) it is more likely to have SFOEWPT for larger mass differences $\Delta m_{H,A}$. Thus, the degenerate mass spectrum $m_H \approx m_{H^\pm} \approx m_A$ depletes the SFOEWPT points. However, when the mass difference is exceedingly large, as in the left and bottom branches, it renders the EW vacuum unstable [67].

VI. COLLIDER AND GRAVITATIONAL WAVE SIGNALS

In this section, we focus on the complementarities between collider and gravitational wave experiments to probe the phase transition pattern in the early Universe. In Fig. 6, we show the scanned points in the $(m_H, c_{\beta-\alpha})$ plane.

⁵However, there is an upper bound on $|\Delta m_H|$. The electroweak symmetry breaking vacuum becomes metastable when the contribution to \mathcal{F}_0 is too sizable.

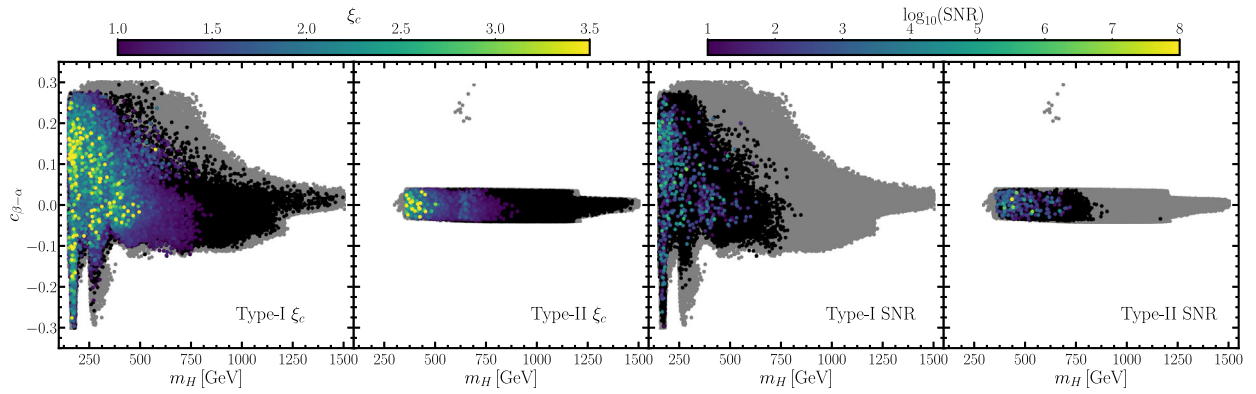


FIG. 6. Scan points in the m_H - $c_{\beta-\alpha}$ plane. The color code is the same as Fig. 5.

The current experimental constraints restrict the 2HDM toward the alignment limit, $c_{\beta-\alpha} \rightarrow 0$.⁶ Although it is possible to have arbitrarily large new scalar masses in the 2HDM, the SFOEWPT and GW observation generally limits these new scalar modes to below the TeV scale [9]. In Fig. 6 (left panel), the $\xi_c > 1$ condition results in a typical upper limit on the heavy scalar mass of $m_H \lesssim 750$ GeV. The lighter the resonance, the higher the order parameter. As shown in Sec. V, this can be explained by an analysis of the theoretically allowed range for the new physics contributions to $\Delta\mathcal{F}_0$. While sizable scalar masses grant only a small vacuum upliftment $\Delta\mathcal{F}_0$, modest scalar masses can display large (and positive) $\Delta\mathcal{F}_0$. This renders strong extra motivation for scalar searches in the 2HDM at the high-luminosity LHC. Hence, in this section, along with the theoretical and current experimental limits, we will discuss the HL-LHC projections of relevant 2HDM searches and contrast with the sensitivity to SFOEWPT and GW observation. In the following, the relevant cross sections are obtained from SCANNERS [34]. It includes a tabulated parametrization of the next-to-next-to-leading-order QCD gluon fusion and bb -associated Higgs production obtained from SUSHI [69,70]. It also encompasses the next-to-leading-order QCD top quark and charged Higgs boson associated production parametrized within HIGGSBOUNDS [41,71–76].

A. Resonant and nonresonant di-Higgs searches

While in the alignment limit, the tree-level Higgs self-coupling matches the SM value $\lambda_{h^3} = \lambda_{h^3}^{\text{SM}}$, the one-loop corrections in the 2HDM can significantly disrupt this equality. In Fig. 7, we show the new physics effects on the triple Higgs coupling $\lambda_{h^3}/\lambda_{h^3}^{\text{SM}}$ at one loop. We observe that

⁶While most experimental limits are generally symmetric with respect to $c_{\beta-\alpha} = 0$, the searches that involve, in particular, the Hhh interaction do not satisfy this form [68]. This asymmetry is more prominent for the type I in the $m_H \gtrsim 2m_h$ regime, where the resonant double Higgs production $H \rightarrow hh$ is kinematically allowed.

the higher-order effects can produce extremely high deviations from the SM, as large as $\lambda_{h^3}/\lambda_{h^3}^{\text{SM}} \approx 7$, even in the alignment limit and in view of the theoretical and experimental constraints. Remarkably, the sizable radiative corrections do not translate in the breakdown of validity for the perturbation theory. Instead, they are a result of new one-loop contributions coming from other types of couplings, such as λ_{hHH} and λ_{hhHH} . The corrections are naturally expected to stabilize beyond one loop, where these new types of effects are already accounted for [77].

The new physics contributions to triple Higgs couplings are occasionally expressed in the effective field theory (EFT) framework, integrating out the heavy modes. Although this approach presents a systematic pathway to include new physics effects in terms of an expansion associated with the new physics scale, it does not generally warrant an appropriate description for the underlying beyond-Standard-Model physics, as it strongly depends on the decoupling of the heavy states [78]. In view of the preference for relative light scalar modes $m_H \lesssim 750$ GeV, producing sizable order parameter $\xi_c > 1$, the EFT does not provide a robust framework to study the preferred SFOEWPT parameter space regime for the 2HDM at the LHC [79]. Hence, as our limits strongly depend on the LHC results, we refrain from using the EFT approach in this study.

The Higgs pair production $pp \rightarrow hh$ provides a direct probe for the Higgs self-coupling at colliders [11,80,81]. However, the limited production rate, large destructive interference between the triangle and box diagrams, and sizable backgrounds make this analysis extremely challenging at the LHC. The ATLAS and CMS high-luminosity projections constrain the triple Higgs coupling at 95% C.L. to [13]

$$0.1 < \lambda_{h^3}/\lambda_{h^3}^{\text{SM}} < 2.3. \quad (29)$$

This limited precision prompts the Higgs self-coupling as a key benchmark for future colliders. In particular, the rapid increase of the gluon luminosity at higher energies translates in a sizable $pp \rightarrow hh$ cross section at the 100 TeV Future Circular Collider. In such a setup, the large number of signal

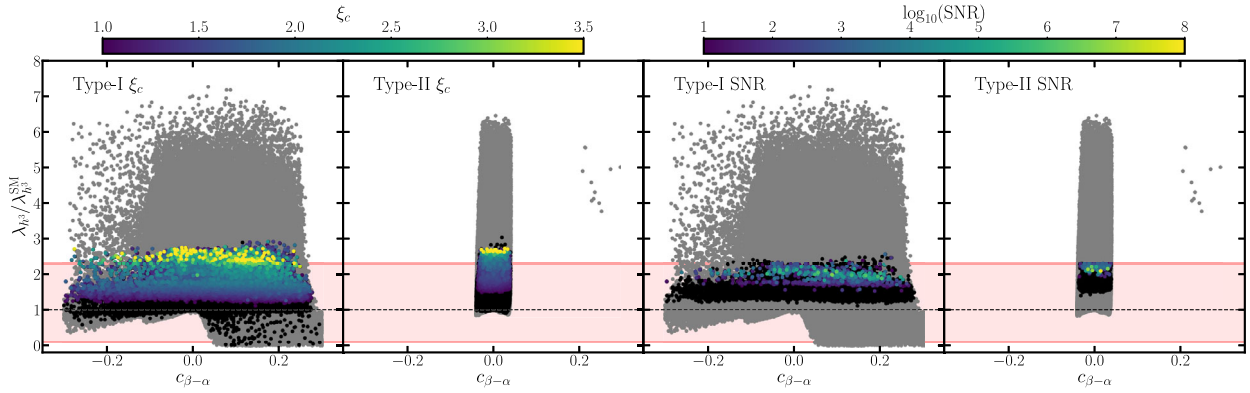


FIG. 7. The triple Higgs coupling normalized to the SM value as a function of $c_{\beta-\alpha}$. The color code is the same as Fig. 5. The HL-LHC projected 95% C.L. sensitivity for nonresonant di-Higgs production is also shown $0.1 < \lambda_{h^3}/\lambda_{h^3}^{\text{SM}} < 2.3$ (light red) [13].

events would transform the di-Higgs production into a precision measurement, allowing for the full kinematic exploration that is central for a better resolution of λ_{h^3} [82]. The improvement to the Higgs self-coupling measurement at higher energy colliders would allow for a more meaningful global fit analysis that is sensitive to a more complete set of new physics modifications to the Higgs potential [83]. Despite the limited experimental constraints, we observe in Fig. 7 that the HL-LHC will be sensitive to a large range of the 2HDM parameter space. In particular, it will be able to probe a substantial fraction of points with a large-order parameter that generally correlates with sizable triple Higgs coupling.

While the HL-LHC will be mostly sensitive to SFOEWPT with large-order parameter $\xi_c \gtrsim 2.5$, LISA will be broadly sensitive to GW signals in the complementary regime $\xi_c \lesssim 2.5$, as shown by the color points of Fig. 7 (right two panels). As explained in Sec. V, extremely large ξ_c leads to the configuration where the system is trapped in the false vacuum precluding successful nucleation. This is reflected in Fig. 7, where the points with large λ_{h^3} (and thus, large ξ_c) in the left two panels do not appear in the right two panels.

Resonant di-Higgs searches provide another prominent probe for the phase transition pattern in the early Universe. As discussed in the last section, SFOEWPT is usually associated with light extra scalars $m_H \lesssim 750$ GeV resulting in a favored energy range for $pp \rightarrow H \rightarrow hh$ production at the LHC. In Fig. 8, in addition to the current theoretical and experimental limits, we present the projected HL-LHC sensitivity at 95% C.L. to the resonant di-Higgs cross section (red dashed line). The results are obtained scaling the current sensitivity presented by ATLAS in Ref. [84], according to the luminosity, to the high-luminosity LHC with $\mathcal{L} = 3 \text{ ab}^{-1}$. This experimental study focuses on the leading $4b$ final state channel. While this analysis explores the gluon fusion production mode, we note that the resonant production through weak boson fusion can provide additional relevant extra sensitivity [85]. We observe in Fig. 8 that the projected resonant Higgs pair production measurement will be able to cover a significant part of the

parameter space with large ξ_c . In contrast, LISA will be sensitive to an important portion of the parameter space probed by the HL-LHC, as well as a relevant fraction of points where the production cross section $pp \rightarrow H \rightarrow hh$ is suppressed.

B. $A \rightarrow ZH$ and $H \rightarrow ZA$ searches

Another important channel is $A \rightarrow ZH$, which is widely discussed in the context of EWPT in the 2HDM [18,86]. As we learned from Sec. V, the left and top branch of Fig. 5 that corresponds to $m_A > m_H$ strongly favors the first-order phase transition due to the large and positive vacuum upliftment contributions from A and possibly H^\pm . The favored parameter space dovetails nicely with the resonant searches through the $A \rightarrow ZH$ channel. Current experimental analyses explore this channel through the decays $H \rightarrow bb$ and $H \rightarrow WW$ with $Z \rightarrow \ell\ell$ [87]. The corresponding constraints projected, according to the luminosity, to the HL-LHC with $\mathcal{L} = 3 \text{ ab}^{-1}$ are shown in Fig. 9 for different channels. We observe that the $H \rightarrow bb$ channel (top panel) provides relevant limits, whereas the $H \rightarrow WW$ mode (bottom panel) results in smaller sensitivity, as it is suppressed by $c_{\beta-\alpha}$. In the type-II scenario, the latter channel does not provide extra sensitivity at the HL-LHC to SFOEWPT. This is due to the stronger constraints on $c_{\beta-\alpha}$ in the type-II 2HDM, pushing it further toward the alignment limit (see, e.g., Fig. 6 or 7). Remarkably, even exploring the dominant channel, where we have $A \rightarrow ZH$ and $H \rightarrow bb$, the sensitivity is still somewhat weak, being limited mostly to the parameter space region $m_H \lesssim 350$ GeV. The main reason is that the bottom quark decay channel quickly becomes subdominant once the scalar mass is beyond the top-pair threshold.⁷ Therefore, the fermionic channel with the top quark will be more

⁷In the type-II scenario, the sensitivity to $H \rightarrow bb$ can extend beyond 350 GeV, as large t_β can enhance the branching ratio $BR(H \rightarrow bb)$ even above the top-pair threshold.

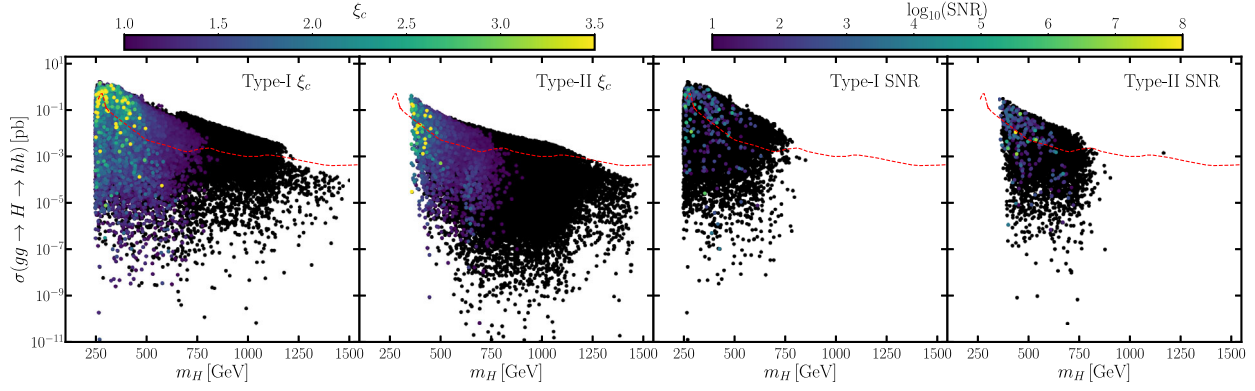


FIG. 8. The cross section $\sigma(gg \rightarrow H) \times \mathcal{BR}(H \rightarrow hh)$ vs m_H . The red dashed line indicates the projected limits from ATLAS with 3 ab^{-1} by scaling the current limits from Ref. [84]. The color code is the same as Fig. 5.

promising in the high-mass region. We will explore the heavy scalar decays to top pairs in the next subsection.

The flipped channel $H \rightarrow ZA$ can *a priori* also provide strong limits [88]. It corresponds to the mass regime $m_H > m_A$, which is associated with the right and bottom branches of Fig. 5. In the right branch, the SFOEWPT is suppressed due to limited positive contributions from heavy scalars to \mathcal{F}_0 . Conversely, the bottom branch could still provide $\xi_c > 1$ points with $t_\beta \rightarrow 1$, as discussed in the previous section. However, this t_β regime precludes possible enhancements in the $A \rightarrow b\bar{b}$ branching fraction. Thus, we do not observe extra sensitivity from this channel to the first-order phase transition at the HL-LHC.

C. Scalar decays to heavy fermions

As observed above, resonant searches with heavy fermionic final states can be crucial for SFOEWPT sensitivity at the HL-LHC. Here, we discuss the projected constraints for both neutral scalars and charged Higgs decays. For the first, we consider the neutral scalar to top-pair search $H/A \rightarrow t\bar{t}$ performed by CMS [89] and scale it, according to the luminosity, to the HL-LHC. Interestingly, this search can display large interference effects between the scalar mediated top-pair production and the SM background; thus, the sensitivity depends on the width of the relevant scalar [90]. The CMS experiment provided the likelihood as a function of the scalar coupling to the top pair for several choices of the scalar mass and width. We scale the likelihood according to the luminosity and linearly interpolate for the scalar mass and width to obtain the upper bound on the coupling for our parameter points. In Fig. 10, we show the branching fraction of A and H decaying into top quarks. The red crosses are the points that can be probed by the HL-LHC. From these plots, we find that the top-pair searches provide a promising search channel to probe SFOEWPT. The $H/A \rightarrow t\bar{t}$ searches will have special importance in the type-II 2HDM, as this scenario presents strong lower bounds on the scalar masses.

For the charged scalars H^\pm , the main search channel at the LHC is the charged scalar associated production with the top and bottom quarks $pp \rightarrow H^\pm tb$, where the H^\pm subsequently decays into the top and bottom quarks $H^\pm \rightarrow tb$ [91]. In Fig. 11, we show the respective cross section times the branching ratio as a function of m_{H^\pm} . The red dashed line indicates the projected limits at the HL-LHC obtained by scaling the current bounds from Ref. [91] according to the luminosity to the HL-LHC with 3 ab^{-1} . We observe that this channel is capable of covering the relevant region of the parameter space that can trigger strong first-order EWPT and produce detectable gravitational wave signals.

D. Combined results

Here, we compare the sensitivity to SFOEWPT for the three aforementioned search channel categories:

- (i) Resonant and nonresonant di-Higgs.
- (ii) $A \rightarrow ZH$ and $H \rightarrow ZA$.
- (iii) $H \rightarrow t\bar{t}$, $A \rightarrow t\bar{t}$, and $H^\pm \rightarrow tb$.

In Fig. 12, we show the fractions of the parameter points from our uniformly random scan that can be covered by distinct search channels (or a combination of them). The left two panels show the case with $\xi_c > 1$, while the right two panels show the case with $\text{SNR} > 10$. The percentage number in each subregion indicates the fraction of the parameter points in that specific subregion. From these Venn diagrams, one can clearly see that the above three categories of search channels are complementary to each other and together can cover a wide portion of the remaining parameter space with strong first-order EWPT. Distinctly, we find that the fermionic modes as well as the di-Higgs channel provide the strongest sensitivity to SFOEWPT and complementary GW signals. For instance, when considering the possibility of probing the large-order parameter $\xi_c > 1$, we observe that the combination of the di-Higgs mode with heavy fermionic decay channels can cover 77% of the remaining type-I scenario and 94% for the type II. At the same time, the widely discussed channel $A(H) \rightarrow ZH(A)$ is still relevant, however, to a smaller

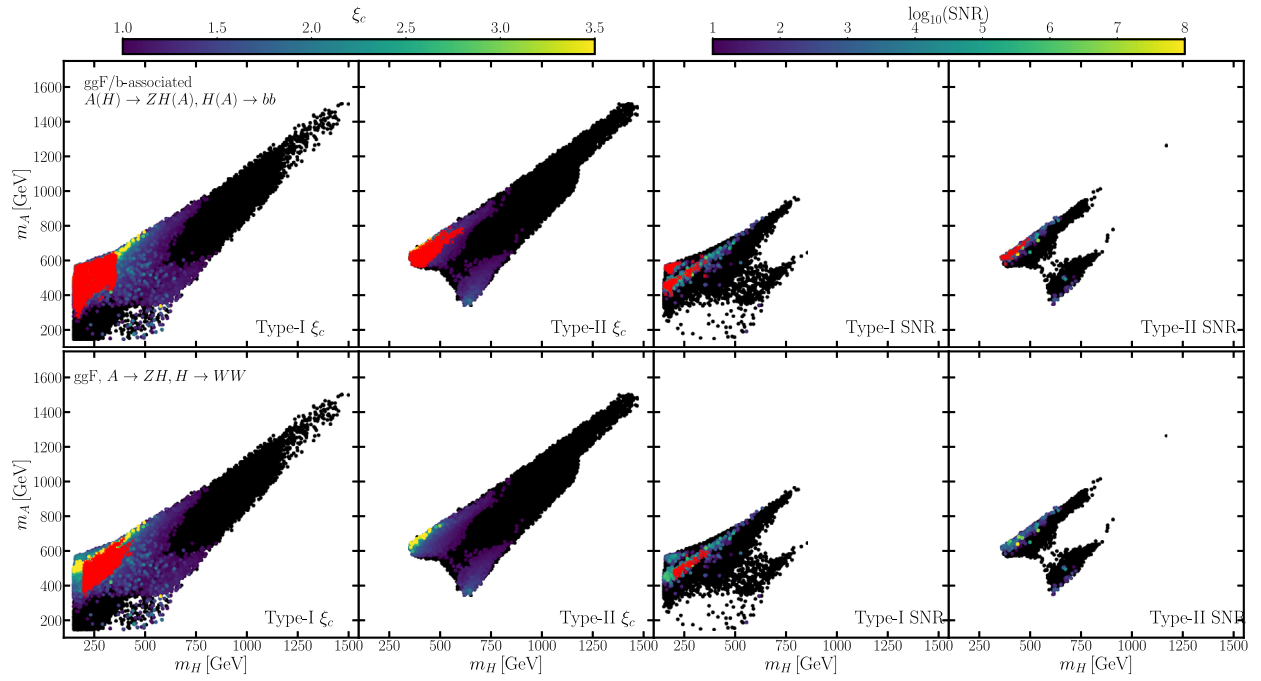


FIG. 9. The $A \rightarrow ZH$ constraints on the $m_H - m_A$ plane. The red crosses are the points that can be probed by the HL-LHC through $A \rightarrow ZH \rightarrow \ell\ell b\bar{b}$ searches, where A is produced through gluon fusion or via b -associated production (top). The projected HL-LHC $A \rightarrow ZH \rightarrow \ell\ell WW$ search is presented with red points, where A is produced via gluon fusion (bottom).

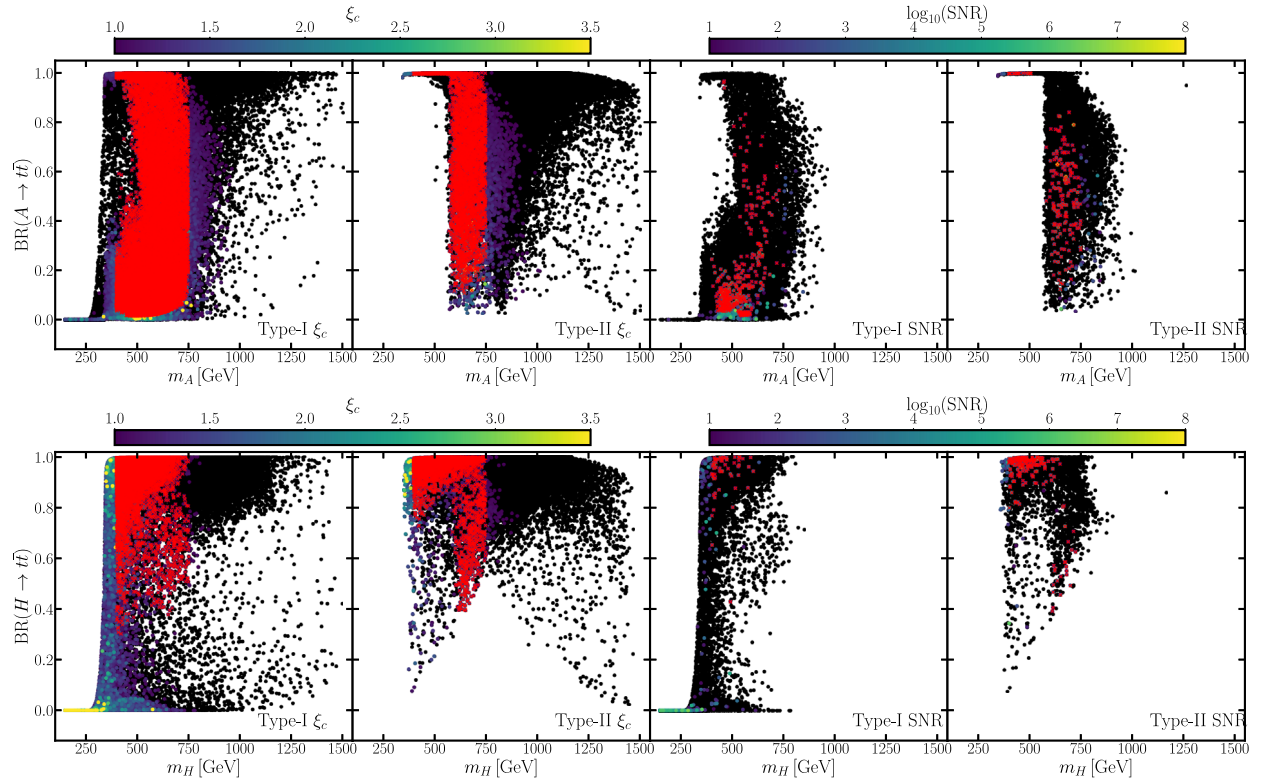


FIG. 10. Branching fraction $\mathcal{BR}(A \rightarrow t\bar{t})$ as a function of m_A (top) and $\mathcal{BR}(H \rightarrow t\bar{t})$ as a function of m_H (bottom). The red crosses are the points with $\xi_c > 1$ (left panels) and $\text{SNR} > 10$ (right panels) that can be probed by the HL-LHC through resonant searches decaying to a top quark pair. The color code is the same as in Fig. 5.

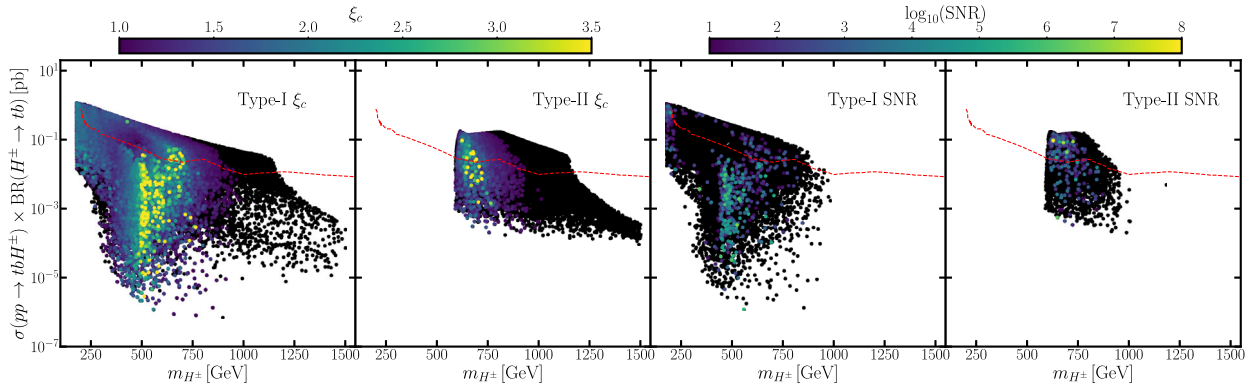


FIG. 11. The cross section $\sigma(pp \rightarrow H^\pm tb) \times \mathcal{BR}(H^\pm \rightarrow tb)$ vs m_{H^\pm} . The red dashed line indicates the projected limits from the HL-LHC. The color code is the same as Fig. 5.

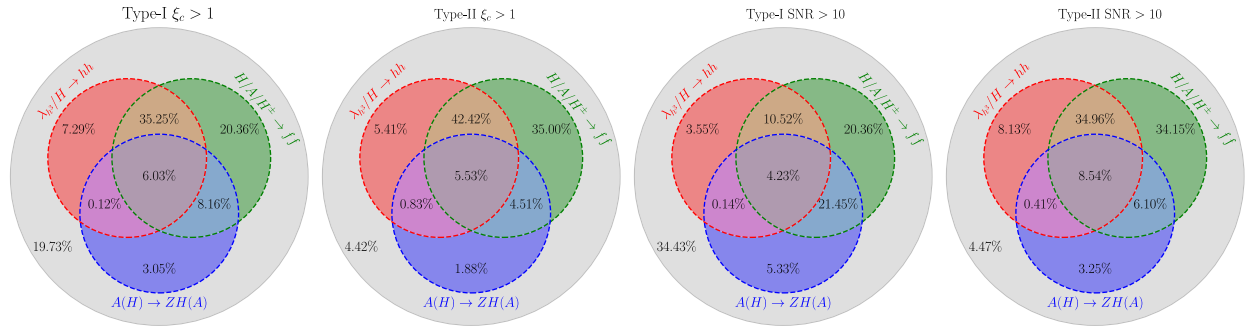


FIG. 12. The summary of the capabilities of the corresponding search channels at the HL-LHC. The number in each region indicates the fraction of parameter points currently allowed by theoretical and experimental constraints from our scan in that particular region.

portion of the parameter space. The sensitivity from $A \rightarrow ZH$ could be, in principle, further enhanced by accounting for the $H \rightarrow t\bar{t}$ channel that is not yet performed by ATLAS and CMS. We leave the referent phenomenological study for future work [92].

In Fig. 13, we present the global HL-LHC and GW complementarities to probe the currently available SFOEWPT parameter space based on our uniformly random scan. We see that the HL-LHC searches will be able to cover $\approx 80\%$ of the remaining $\xi_c > 1$ parameter

space for the type-I 2HDM and an impressive $\approx 96\%$ for the type-II scenario. At the same time, LISA will be able to access a complementary parameter space region with a typically low production cross section at the HL-LHC for the considered processes. The requirement for small scalar masses to induce positive contributions for \mathcal{F}_0 plays a crucial role in the sizable HL-LHC sensitivity to SFOEWPT. These fractions present only a lower bound. Adding other complementary 2HDM search channels at the HL-LHC, beyond the three considered classes, should push the quoted sensitivities to an even higher level.

VII. SUMMARY

Reconstructing the shape of the Higgs potential is crucial for understanding the origin of mass and the thermal history of electroweak symmetry breaking in our Universe. In this work, we explore the complementarity between collider and gravitational wave experiments to probe the scalar potential in the 2HDM. We scrutinize fundamental ingredients in the profile of the Higgs potential, namely, the barrier formation and upliftment of the true vacuum that promote the transmutation of phase transition from the smooth crossover to the strong first-order phase transition. In addition, accounting for the theoretical and current experimental measurements, we study the prospects for

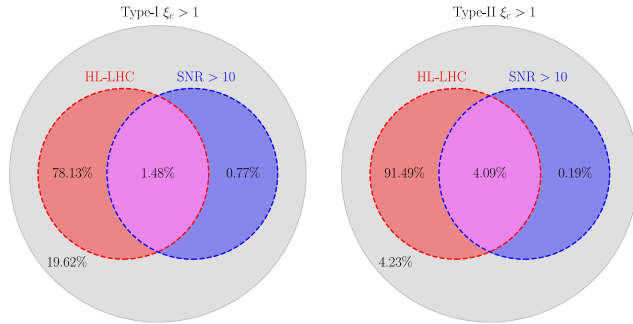


FIG. 13. The summary of the capabilities of the HL-LHC and GW experiments. The number in each region indicates the fraction of parameter points from our scan in that particular region.

the HL-LHC to probe the $\xi_c > 1$ regime focusing on three prominent classes of searches [resonant and nonresonant di-Higgs, $A(H) \rightarrow ZH(A)$, and heavy scalar decays to fermions] and contrasted with the GW sensitivity at LISA. We summarize our novel results as follows:

- (i) When comparing the parameter space points that survive the theoretical and experimental constraints for type-I and type-II 2HDM, these scenarios result in an akin phase transition pattern.
- (ii) The barrier formation in the Higgs potential of the 2HDM is driven by the one-loop and thermal corrections, with the dominance of the one-loop terms for large-order parameter $\xi_c > 1$.
- (iii) The strength of phase transition is correlated with the upliftment of the true vacuum with respect to the symmetric one at zero temperature [22,61,62]. This arises as a result of the dominance of the one-loop effects with respect to the thermal corrections for $\xi_c > 1$. Based on this result, we shed light on the phase transition pattern analytically. In particular, we observe that larger vacuum upliftment is favored for lower scalar masses which is in accordance with the results from a generic discussion in [9]. This provides strong extra motivation for scalar searches at the LHC. Besides scalar masses below the TeV scale, the analytical structure of the new physics effects on the vacuum upliftment, leading to SFOEWPT, result in a peculiar hierarchy of masses among the new scalar modes. These findings work as a guide for collider and gravitational wave studies.
- (iv) We obtain that the scalar decays to heavy fermions ($H, A, H^\pm \rightarrow tt, tb$) are the most promising smoking gun signature for SFOEWPT at the HL-LHC, followed by the di-Higgs searches. Based on the projections from the current ATLAS and CMS searches, the widely discussed channel $A(H) \rightarrow ZH(A)$ is still relevant, whereas to a smaller fraction of the parameter space. The main reason for such an observation is that the current experiments focus on the bb and WW decay channels [87]. These two decay modes only cover a small portion of the parameter space. We leave for future work a direct phenomenological comparison of the gluon fusion $gg \rightarrow H(A)$ and $A(H) \rightarrow ZH(A)$ channels, considering the promising $t\bar{t}$ heavy fermion final states [92].
- (v) In contrast to the HL-LHC, LISA is going to be sensitive to a significantly smaller parameter space region, whereas it renders to complementary sensitivities where the correspondent LHC cross section is suppressed. Based on our parameter space scan, the combination of the LHC searches with

gravitational wave studies presents exciting prospects to probe the vast majority of first-order phase transition points in the 2HDM. Adding other complementary 2HDM search channels at the HL-LHC, beyond the three considered classes, should push new physics sensitivity to an even higher level.

In conclusion, the study of the thermal history of electroweak symmetry breaking is a crucial challenge for particle physics and cosmology. We demonstrate that the well-motivated 2HDM leads to a rich phase transition pattern favoring SFOEWPT below the TeV scale. This renders exciting physics prospects at the HL-LHC and upcoming gravitational wave experiments, such as LISA.

ACKNOWLEDGMENTS

We thank Maria Cepeda and Alessia Saggio for clarifying some details of Ref. [88]. D. G., A. K., and Y. W. thank the U.S. Department of Energy for the financial support, under Grant No. DE-SC 0016013. Some computing for this project was performed at the High Performance Computing Center at Oklahoma State University, supported in part by the National Science Foundation Grant No. OAC-1531128.

APPENDIX: POTENTIAL PARAMETERS IN THE 2HDM

In this Appendix, we express the masses m_{11}^2, m_{22}^2 and coupling parameters $\lambda_1 \dots \lambda_5$ in terms of the parameters $m_h, m_H, m_A, m_{H^\pm}, \beta, \alpha$, and m_{12}^2 used throughout this manuscript:

$$\lambda_1 v^2 = \frac{1}{c_\beta} (s_\alpha^2 m_h^2 + c_\alpha^2 m_H^2 - m_{12}^2 \tan \beta), \quad (\text{A1a})$$

$$\lambda_2 v^2 = \frac{1}{s_\beta^2} (c_\alpha^2 m_h^2 + s_\alpha^2 m_H^2 - m_{12}^2 / \tan \beta), \quad (\text{A1b})$$

$$\lambda_3 v^2 = 2m_{H^\pm}^2 + \frac{s_{2\alpha}}{s_{2\beta}} (m_H^2 - m_h^2) - \frac{m_{12}^2}{s_\beta c_\beta}, \quad (\text{A1c})$$

$$\lambda_4 v^2 = m_A^2 - 2m_{H^\pm}^2 + \frac{m_{12}^2}{s_\beta c_\beta}, \quad (\text{A1d})$$

$$\lambda_5 v^2 = \frac{m_{12}^2}{s_\beta c_\beta} - m_A^2, \quad (\text{A1e})$$

$$m_{11}^2 = m_{12}^2 \tan \beta - \frac{m_H^2 c_\alpha}{2 c_\beta} c_{\beta-\alpha} + \frac{m_h^2 s_\alpha}{2 c_\beta} s_{\beta-\alpha}, \quad (\text{A1f})$$

$$m_{22}^2 = \frac{m_{12}^2}{\tan \beta} - \frac{m_H^2 s_\alpha}{2 s_\beta} c_{\beta-\alpha} - \frac{m_h^2 c_\alpha}{2 s_\beta} s_{\beta-\alpha}. \quad (\text{A1g})$$

- [1] K. Kajantie, M. Laine, K. Rummukainen, and M. E. Shaposhnikov, Is There a Hot Electroweak Phase Transition at $m_H \gtrsim m_W$?, *Phys. Rev. Lett.* **77**, 2887 (1996).
- [2] Planck Collaboration, Planck 2015 results. XIII. Cosmological parameters, *Astron. Astrophys.* **594**, A13 (2016).
- [3] A. D. Sakharov, Violation of CP invariance, C asymmetry, and baryon asymmetry of the Universe, *Pis'ma Sov. Phys. Usp.* **34**, 392 (1991).
- [4] P. Huet and E. Sather, Electroweak baryogenesis and standard model CP violation, *Phys. Rev. D* **51**, 379 (1995).
- [5] M. Trodden, Electroweak baryogenesis, *Rev. Mod. Phys.* **71**, 1463 (1999).
- [6] A. G. Cohen, D. B. Kaplan, and A. E. Nelson, Progress in electroweak baryogenesis, *Annu. Rev. Nucl. Part. Sci.* **43**, 27 (1993).
- [7] M. Carena, M. Quiros, and C. E. M. Wagner, Opening the window for electroweak baryogenesis, *Phys. Lett. B* **380**, 81 (1996).
- [8] D. E. Morrissey and M. J. Ramsey-Musolf, Electroweak baryogenesis, *New J. Phys.* **14**, 125003 (2012).
- [9] M. J. Ramsey-Musolf, The electroweak phase transition: A collider target, *J. High Energy Phys.* **09** (2020) 179.
- [10] O. J. P. Eboli, G. C. Marques, S. F. Novaes, and A. A. Natale, Twin Higgs boson production, *Phys. Lett. B* **197**, 269 (1987).
- [11] T. Plehn, M. Spira, and P. M. Zerwas, Pair production of neutral Higgs particles in gluon-gluon collisions, *Nucl. Phys.* **B479**, 46 (1996).
- [12] J. M. No and M. Ramsey-Musolf, Probing the Higgs portal at the LHC through resonant di-Higgs production, *Phys. Rev. D* **89**, 095031 (2014).
- [13] M. Cepeda *et al.*, Report from Working Group 2: Higgs physics at the HL-LHC and HE-LHC, *CERN Yellow Rep. Monogr.* **7**, 221 (2019).
- [14] ATLAS Collaboration, Search for pair production of Higgs bosons in the $b\bar{b}b\bar{b}$ final state using proton-proton collisions at $\sqrt{s} = 13$ TeV with the ATLAS detector, *J. High Energy Phys.* **01** (2019) 030.
- [15] LISA Collaboration, Laser interferometer space antenna, *arXiv:1702.00786*.
- [16] C. Grojean and G. Servant, Gravitational waves from phase transitions at the electroweak scale and beyond, *Phys. Rev. D* **75**, 043507 (2007).
- [17] C. Caprini *et al.*, Detecting gravitational waves from cosmological phase transitions with LISA: An update, *J. Cosmol. Astropart. Phys.* **03** (2020) 024.
- [18] G. C. Dorsch, S. J. Huber, and J. M. No, A strong electroweak phase transition in the 2HDM after LHC8, *J. High Energy Phys.* **10** (2013) 029.
- [19] P. Basler, M. Krause, M. Mühlleitner, J. Wittbrodt, and A. Wlotzka, Strong first order electroweak phase transition in the CP -conserving 2HDM revisited, *J. High Energy Phys.* **02** (2017) 121.
- [20] G. C. Dorsch, S. J. Huber, K. Mimasu, and J. M. No, Hierarchical versus degenerate 2HDM: The LHC run 1 legacy at the onset of run 2, *Phys. Rev. D* **93**, 115033 (2016).
- [21] J. Bernon, L. Bian, and Y. Jiang, A new insight into the phase transition in the early Universe with two Higgs doublets, *J. High Energy Phys.* **05** (2018) 151.
- [22] G. Dorsch, S. Huber, K. Mimasu, and J. No, The Higgs vacuum uplifted: Revisiting the electroweak phase transition with a second Higgs doublet, *J. High Energy Phys.* **12** (2017) 086.
- [23] J. O. Andersen, T. Gorda, A. Helset, L. Niemi, T. V. I. Tenkanen, A. Tranberg, A. Vuorinen, and D. J. Weir, Non-perturbative Analysis of the Electroweak Phase Transition in the Two Higgs Doublet Model, *Phys. Rev. Lett.* **121**, 191802 (2018).
- [24] K. Kainulainen, V. Keus, L. Niemi, K. Rummukainen, T. V. I. Tenkanen, and V. Vaskonen, On the validity of perturbative studies of the electroweak phase transition in the two Higgs doublet model, *J. High Energy Phys.* **06** (2019) 075.
- [25] W. Su, A. G. Williams, and M. Zhang, Strong first order electroweak phase transition in 2HDM confronting future Z & Higgs factories, *J. High Energy Phys.* **04** (2021) 219.
- [26] H. Davoudiasl, I. M. Lewis, and M. Sullivan, Multi-TeV signals of baryogenesis in a Higgs troika model, *Phys. Rev. D* **104**, 015024 (2021).
- [27] T. Biekötter, S. Heinemeyer, J. M. No, M. O. Olea, and G. Weiglein, Fate of electroweak symmetry in the early Universe: Non-restoration and trapped vacua in the N2HDM, *J. Cosmol. Astropart. Phys.* **06** (2021) 018.
- [28] M. Aoki, T. Komatsu, and H. Shibuya, Possibility of multi-step electroweak phase transition in the two Higgs doublet models, *arXiv:2106.03439*.
- [29] G. C. Branco, P. M. Ferreira, L. Lavoura, M. N. Rebelo, M. Sher, and J. P. Silva, Theory and phenomenology of two-Higgs-doublet models, *Phys. Rep.* **516**, 1 (2012).
- [30] S. L. Glashow and S. Weinberg, Natural conservation laws for neutral currents, *Phys. Rev. D* **15**, 1958 (1977).
- [31] E. A. Paschos, Diagonal neutral currents, *Phys. Rev. D* **15**, 1966 (1977).
- [32] J. F. Gunion and H. E. Haber, The CP conserving two Higgs doublet model: The approach to the decoupling limit, *Phys. Rev. D* **67**, 075019 (2003).
- [33] R. Coimbra, M. O. P. Sampaio, and R. Santos, SCANNERS: Constraining the phase diagram of a complex scalar singlet at the LHC, *Eur. Phys. J. C* **73**, 2428 (2013).
- [34] M. Mühlleitner, M. O. P. Sampaio, R. Santos, and J. Wittbrodt, SCANNERS: Parameter scans in extended scalar sectors, *Eur. Phys. J. C* **82**, 198 (2022).
- [35] B. W. Lee, C. Quigg, and H. B. Thacker, Weak interactions at very high energies: The role of the Higgs boson mass, *Phys. Rev. D* **16**, 1519 (1977).
- [36] S. Kanemura, T. Kubota, and E. Takasugi, Lee-Quigg-Thacker bounds for Higgs boson masses in a two doublet model, *Phys. Lett. B* **313**, 155 (1993).
- [37] I. F. Ginzburg and I. P. Ivanov, Tree-level unitarity constraints in the most general 2HDM, *Phys. Rev. D* **72**, 115010 (2005).
- [38] I. P. Ivanov, M. Köpke, and M. Mühlleitner, Algorithmic boundedness-from-below conditions for generic scalar potentials, *Eur. Phys. J. C* **78**, 413 (2018).
- [39] W. G. Hollik, G. Weiglein, and J. Wittbrodt, Impact of vacuum stability constraints on the phenomenology of supersymmetric models, *J. High Energy Phys.* **03** (2019) 109.

- [40] P. M. Ferreira, M. Mühlleitner, R. Santos, G. Weiglein, and J. Wittbrodt, Vacuum instabilities in the N2HDM, *J. High Energy Phys.* **09** (2019) 006.
- [41] P. Bechtle, D. Dercks, S. Heinemeyer, T. Klingl, T. Stefaniak, G. Weiglein, and J. Wittbrodt, HIGGSBOUNDS-5: Testing Higgs sectors in the LHC 13 TeV era, *Eur. Phys. J. C* **80**, 1211 (2020).
- [42] P. Bechtle, S. Heinemeyer, T. Klingl, T. Stefaniak, G. Weiglein, and J. Wittbrodt, HIGGSIGNALS-2: Probing new physics with precision Higgs measurements in the LHC 13 TeV era, *Eur. Phys. J. C* **81**, 145 (2021).
- [43] S. Coleman and E. Weinberg, Radiative corrections as the origin of spontaneous symmetry breaking, *Phys. Rev. D* **7**, 1888 (1973).
- [44] C.-W. Chiang, M. J. Ramsey-Musolf, and E. Senaha, Standard model with a complex scalar singlet: Cosmological implications and theoretical considerations, *Phys. Rev. D* **97**, 015005 (2018).
- [45] O. Gould and T. V. I. Tenkanen, On the perturbative expansion at high temperature and implications for cosmological phase transitions, *J. High Energy Phys.* **06** (2021) 069.
- [46] J. E. Camargo-Molina, A. P. Morais, R. Pasechnik, M. O. P. Sampaio, and J. Wessén, All one-loop scalar vertices in the effective potential approach, *J. High Energy Phys.* **08** (2016) 073.
- [47] P. B. Arnold and O. Espinosa, The effective potential and first order phase transitions: Beyond leading-order, *Phys. Rev. D* **47**, 3546 (1993).
- [48] T. Matsubara, A new approach to quantum statistical mechanics, *Prog. Theor. Phys.* **14**, 351 (1955).
- [49] M. Quiros, Finite temperature field theory and phase transitions [arXiv:hep-ph/9901312](https://arxiv.org/abs/hep-ph/9901312).
- [50] H. H. Patel and M. J. Ramsey-Musolf, Baryon washout, electroweak phase transition, and perturbation theory, *J. High Energy Phys.* **07** (2011) 029.
- [51] C. Wainwright, S. Profumo, and M. J. Ramsey-Musolf, Gravity waves from a cosmological phase transition: Gauge artifacts and daisy resummations, *Phys. Rev. D* **84**, 023521 (2011).
- [52] D. Metaxas and E. J. Weinberg, Gauge independence of the bubble nucleation rate in theories with radiative symmetry breaking, *Phys. Rev. D* **53**, 836 (1996).
- [53] M. Garny and T. Konstandin, On the gauge dependence of vacuum transitions at finite temperature, *J. High Energy Phys.* **07** (2012) 189.
- [54] S. Arunasalam and M. J. Ramsey-Musolf, Tunneling potentials for the tunneling action: Gauge invariance, [arXiv:2105.07588](https://arxiv.org/abs/2105.07588).
- [55] N. K. Nielsen, On the gauge dependence of spontaneous symmetry breaking in gauge theories, *Nucl. Phys.* **B101**, 173 (1975).
- [56] A. D. Linde, Fate of the false vacuum at finite temperature: Theory and applications, *Phys. Lett.* **100B**, 37 (1981).
- [57] S. R. Coleman, The fate of the false vacuum. 1. Semi-classical theory, *Phys. Rev. D* **15**, 2929 (1977).
- [58] C. L. Wainwright, COSMOTRANSITIONS: Computing cosmological phase transition temperatures and bubble profiles with multiple fields, *Comput. Phys. Commun.* **183**, 2006 (2012).
- [59] J. M. Moreno, M. Quiros, and M. Seco, Bubbles in the supersymmetric standard model, *Nucl. Phys.* **B526**, 489 (1998).
- [60] C. Caprini *et al.*, Science with the space-based interferometer eLISA. II: Gravitational waves from cosmological phase transitions, *J. Cosmol. Astropart. Phys.* **04** (2016) 001.
- [61] W. Huang, Z. Kang, J. Shu, P. Wu, and J. M. Yang, New insights in the electroweak phase transition in the NMSSM, *Phys. Rev. D* **91**, 025006 (2015).
- [62] C. Harman and S. Huber, Does zero temperature decide on the nature of the electroweak phase transition?, *J. High Energy Phys.* **06** (2016) 005.
- [63] D. J. H. Chung, A. J. Long, and L.-T. Wang, 125 GeV Higgs boson and electroweak phase transition model classes, *Phys. Rev. D* **87**, 023509 (2013).
- [64] M. Reichert, A. Eichhorn, H. Gies, J. M. Pawłowski, T. Plehn, and M. M. Scherer, Probing baryogenesis through the Higgs boson self-coupling, *Phys. Rev. D* **97**, 075008 (2018).
- [65] W. Grimus, L. Lavoura, O. M. Ogreid, and P. Osland, A precision constraint on multi-Higgs-doublet models, *J. Phys. G* **35**, 075001 (2008).
- [66] J. M. Gerard and M. Herquet, A Twisted Custodial Symmetry in the Two-Higgs-Doublet Model, *Phys. Rev. Lett.* **98**, 251802 (2007).
- [67] I. P. Ivanov and J. P. Silva, Tree-level metastability bounds for the most general two Higgs doublet model, *Phys. Rev. D* **92**, 055017 (2015).
- [68] ATLAS Collaboration, Combination of searches for Higgs boson pairs in pp collisions at $\sqrt{s} = 13$ TeV with the ATLAS detector, *Phys. Lett. B* **800**, 135103 (2020).
- [69] R. V. Harlander, S. Liebler, and H. Mantler, SUSHI: A program for the calculation of Higgs production in gluon fusion and bottom-quark annihilation in the Standard Model and the MSSM, *Comput. Phys. Commun.* **184**, 1605 (2013).
- [70] R. V. Harlander, S. Liebler, and H. Mantler, SusHi Bento: Beyond NNLO and the heavy-top limit, *Comput. Phys. Commun.* **212**, 239 (2017).
- [71] E. L. Berger, T. Han, J. Jiang, and T. Plehn, Associated production of a top quark and a charged Higgs boson, *Phys. Rev. D* **71**, 115012 (2005).
- [72] S. Dittmaier, M. Kramer, M. Spira, and M. Walser, Charged-Higgs-boson production at the LHC: NLO supersymmetric QCD corrections, *Phys. Rev. D* **83**, 055005 (2011).
- [73] M. Flechl, R. Klees, M. Kramer, M. Spira, and M. Ubiali, Improved cross-section predictions for heavy charged Higgs boson production at the LHC, *Phys. Rev. D* **91**, 075015 (2015).
- [74] C. Degrande, M. Ubiali, M. Wiesemann, and M. Zaro, Heavy charged Higgs boson production at the LHC, *J. High Energy Phys.* **10** (2015) 145.
- [75] LHC Higgs Cross Section Working Group, *Handbook of LHC Higgs Cross Sections: 4. Deciphering the Nature of the Higgs Sector*, edited by D. de Florian, C. Grojean, F. Maltoni, C. Mariotti, A. Nikitenko, M. Pieri, P. Savard, M. Schumacher, and R. Tanaka (CERN, Geneva, 2017).
- [76] C. Degrande, R. Frederix, V. Hirschi, M. Ubiali, M. Wiesemann, and M. Zaro, Accurate predictions for charged

- Higgs production: Closing the $m_{H^\pm} \sim m_t$ window, *Phys. Lett. B* **772**, 87 (2017).
- [77] S. Kanemura, S. Kiyoura, Y. Okada, E. Senaha, and C. P. Yuan, New physics effect on the Higgs self-coupling, *Phys. Lett. B* **558**, 157 (2003).
- [78] T. Appelquist and J. Carazzone, Infrared singularities and massive fields, *Phys. Rev. D* **11**, 2856 (1975).
- [79] M. Postma and G. White, Cosmological phase transitions: Is effective field theory just a toy?, *J. High Energy Phys.* **03** (2021) 280.
- [80] O. boli, G. Marques, S. Novaes, and A. Natale, Twin Higgs-boson production, *Phys. Lett. B* **197**, 269 (1987).
- [81] M. J. Dolan, C. Englert, and M. Spannowsky, Higgs self-coupling measurements at the LHC, *J. High Energy Phys.* **10** (2012) 112.
- [82] D. Gonçalves, T. Han, F. Kling, T. Plehn, and M. Takeuchi, Higgs boson pair production at future hadron colliders: From kinematics to dynamics, *Phys. Rev. D* **97**, 113004 (2018).
- [83] A. Biekötter, D. Gonçalves, T. Plehn, M. Takeuchi, and D. Zerwas, The global Higgs picture at 27 TeV, *SciPost Phys.* **6**, 024 (2019).
- [84] ATLAS Collaboration, Search for pair production of Higgs bosons in the $b\bar{b}b\bar{b}$ final state using proton-proton collisions at $\sqrt{s} = 13$ TeV with the ATLAS detector, *J. High Energy Phys.* **01** (2019) 030.
- [85] R. K. Barman, C. Englert, D. Gonçalves, and M. Spannowsky, Di-Higgs resonance searches in weak boson fusion, *Phys. Rev. D* **102**, 055014 (2020).
- [86] G. C. Dorsch, S. J. Huber, K. Mimasu, and J. M. No, Echoes of the Electroweak Phase Transition: Discovering a Second Higgs Doublet through $A_0 \rightarrow ZH_0$, *Phys. Rev. Lett.* **113**, 211802 (2014).
- [87] ATLAS Collaboration, Search for a heavy Higgs boson decaying into a Z boson and another heavy Higgs boson in the $\ell\ell b\bar{b}$ and $\ell\ell WW$ final states in pp collisions at $\sqrt{s} = 13$ TeV with the ATLAS detector, *Eur. Phys. J. C* **81**, 396 (2021).
- [88] CMS Collaboration, Search for new neutral Higgs bosons through the $H \rightarrow ZA \rightarrow \ell^+\ell^-b\bar{b}$ process in pp collisions at $\sqrt{s} = 13$ TeV, *J. High Energy Phys.* **03** (2020) 055.
- [89] CMS Collaboration, Search for heavy Higgs bosons decaying to a top quark pair in proton-proton collisions at $\sqrt{s} = 13$ TeV, *J. High Energy Phys.* **04** (2020) 171.
- [90] D. Dicus, A. Stange, and S. Willenbrock, Higgs decay to top quarks at hadron colliders, *Phys. Lett. B* **333**, 126 (1994).
- [91] ATLAS Collaboration, Search for charged Higgs bosons decaying into a top quark and a bottom quark at $\sqrt{s} = 13$ TeV with the ATLAS detector, *J. High Energy Phys.* **06** (2021) 145.
- [92] D. Gonçalves, A. Kaladharan, and Y. Wu (to be published).